ABSTRACT

Title of Document:	EFFECTS OF ADSORBATES ON THE ELECTRONIC PROPERTIES OF GRAPHENE
	Shudong Xiao, Doctor of Philosophy, 2012
Directed By:	Professor, Michael S. Fuhrer, Department of Physics.

Graphene, an atom-thick sheet of carbon, is a novel two-dimensional material in which the low-energy electrons behave as massless Dirac fermions. This thesis explores the effects of adsorbates on the electronic properties graphene by adsorption in controlled environment in ultra-high vacuum (UHV), coupled with *in situ* measurement of transport properties. Two types of adsorbates on graphene are investigated. First, the effects of charged impurity scattering are studied by controlled adsorption of potassium on bilayer graphene at low temperature in UHV. The results indicate that the magnitude of charged-impurity scattering in bilayer graphene is similar to that in single layer graphene, and in good agreement with theory. The widely observed lower mobility in bilayer graphene on SiO_2 is likely due to another source of disorder. Second, the dielectric screening of bilayer graphene is modified by deposition of ice overlayers at low temperature in UHV. No screening effect is observed in pristine bilayer graphene. However, ice overlayers significantly increase the mobility of potassium-doped bilayer graphene through

screening of potassium ions. Together, the ice deposition experiments demonstrate the existence of screening effect in bilayer graphene and support that charge impurities are not the dominant scatters in pristine bilayer graphene on SiO_2. The screening of adsorbed potassium ions on single-layer graphene is also investigated both experimentally and theoretically. The increase in mobility upon ice deposition is much larger than expected assuming ice's bulk relative dielectric constant of 3.2. A simple model assuming stronger local screening near potassium ions is proposed which can explain the experimental observations. Temperature-dependent studies of electronic transport in the system of coadsorbed potassium and ice show that graphene's resistivity is sensitive to phase transitions in overlayers as well as desorption, opening new opportunities to study surface phases with electronic measurements.

EFFECTS OF ADSORBATES ON THE ELECTRONIC PROPERTIES OF GRAPHENE

By

Shudong Xiao

Dissertation submitted to the Faculty of the Graduate School of the
University of Maryland, College Park, in partial fulfillment
of the requirements for the degree of
Doctor of Philosophy
2012

Advisory Committee:
Professor Michael S. Fuhrer, Chair
Professor Theodore L. Einstein
Associate Professor Min Ouyang
Associate Research Scientist William G. Cullen
Professor Janice E. Reutt-Robey

Dedication

To my parents Xiao Zhenqi and Dong Xiufeng,

my wife Wu Sana and my son Xiao Jiawei (Gavin)

Acknowledgements

Completing my Ph.D. degree is a long and challenging journey through which I have traveled with support and encouragement from many people that I would like to acknowledge.

First and foremost, I express my sincere gratitude to my advisor Professor Michael S. Fuhrer for his continuous support and guidance to my research. He is an energetic scientist with great insights, who has introduced many exciting research topics to me and always directed my projects to the right direction. I have been fortunate to have an enthusiastic and patient advisor and I have the pleasure to work with him.

I would like to thank the members of my dissertation committee, Prof. Theodore L. Einstein, Prof. Min Ouyang, Dr. William G. Cullen and Prof. Janice E. Reutt-Robey, for their guidance that leads to the completion of this thesis.

I am indebted to Prof. Ellen D. Williams, who has provided equipment support for my experiments. I would like to give special thanks to former members of her group, Prof. Masahiro Ishigami and Dr. Jian-Hao Chen. They have built the UHV transport system and taught me a lot of laboratory skills.

I would like to thank Dr. William G. Cullen, Dr. Chaun Jang and Dr. Jun Yan for useful discussions on the UHV experiments.

I would like to thank all the people who have helped me in finishing the work in this thesis: David Tobias, Gokhan Esen, Tareq Ghanem, Adrian Southard, Daniel Lenski, Enrique Cobas, SungJae Cho, Alexandra Curtin, Xinghan (Harold) Cai, Jack Hellerstedt, Liang Li, Jinglei Ping, Jacob Tosado, Dohun Kim, Claudia Ojeda, Jun Yan, Wenzhong

Bao, Yilin Wang, Brad Conrad, Tracy Moore, Kristen Burson, Michelle Zimmermann and Mahito Yamamoto.

I would like to thank Prof. Sankar Das Sarma, Dr. Shaffique Adam, Dr. Euyheon Hwang and Prof. Enrico Rossi for sharing of theoretical insights.

My gratitude is also extended to all my friends. I appreciate what they have done for me and for my family during my Ph.D. program and cherish all the wonderful memories. Without their understanding and encouragement, I would not have made my way so far.

Table of Contents

List of Figures

Chapter 1 Introduction to graphene: a great unexpectation

1.1 Introduction

Graphene, an atom-thick sheet of carbon, has been a classical example used to demonstrate tight-binding calculation in solid state physics for more than 60 years[1]. Further theoretical study discovered a fascinating point that the band structure of graphene can be expanded near Fermi surface, where the tight-binding equation becomes two-dimensional (2D) massless Dirac equation[2, 3]. However, with a then-common belief that two-dimensional crystal should not exist, the theoretical work was only regarded as a starting point for understanding graphene-based materials, e.g., graphite, carbon nanotubes and C_{60}.

In 2004, a ground-breaking work, extracting single-layer graphene from bulk graphite, surprised the scientific community. In this experimental approach[4], common Scotch tape was used to exfoliate bulk graphite and transfer graphene to thin SiO_2 on Si substrates. The success of such a simple technique was totally unexpected, especially after a number of complicated experiments had failed in this direction since 1990s[5-8]. Once mechanically exfoliated, graphene is only bonded to the substrate by Van de Waals force. The weak interaction with the substrate allows graphene to keep its intrinsic band structure, and the insulating nature of the substrate allows electronic experiments on graphene. In particular, the SiO_2 and Si substrate act as gate dielectric and gate electrode respectively, allowing ambipolar tuning of the charge carrier density in graphene. Such experiments led to the observation of the anomalous half-integer quantum Hall effect[9,

10], a unique behavior of massless Dirac fermions, providing the first direct evidence of the theoretical prediction of chiral Dirac quasi-particles in graphene.

1.2 Tight-binding calculation of graphene bandstructure

The connection between condensed matter experiments and the Dirac equation in graphene physics, however formidable as it may sound, originates from rather basic tight-binding calculations. Carbon has four valence electrons, three of which form the sp^2-hybridized or σ bonds through the linear combinations of s, p_x and p_y orbitals. Their energy levels are called σ bands. The sp^2 bonds lie in the graphene plane with a carbon-carbon bond length a_0=1.42 Å. Although the sp^2 bonds control the arrangement of the carbon atoms in the 2D crystal, the corresponding σ bonding (anti-bonding) bands lie far below (above) the Fermi surface and are unimportant in the low-energy electronic properties of graphene. The graphene honeycomb lattice consists of two Bravais sublattices, as illustrated by the black and gray dots in Figure 1.1A. Therefore, each unit cell of the graphene crystal consists of two carbon atoms. The shaded area in Figure 1.1A is one way to choose the unit cell with $\boldsymbol{a_1}$ and $\boldsymbol{a_2}$ as the lattice vectors. The two carbon atoms are labeled as 1 and 2. The fourth valence electron of the carbon atom occupies the p_z or π orbital and only weakly interacts with other carbon atoms' p_z orbitals. The energy levels from the p_z orbitals are called π bands. The π bands are the lowest-lying energy bands in neutral graphene, and it is in the π bands that theoretical calculation first revealed the existence of massless Dirac fermions.

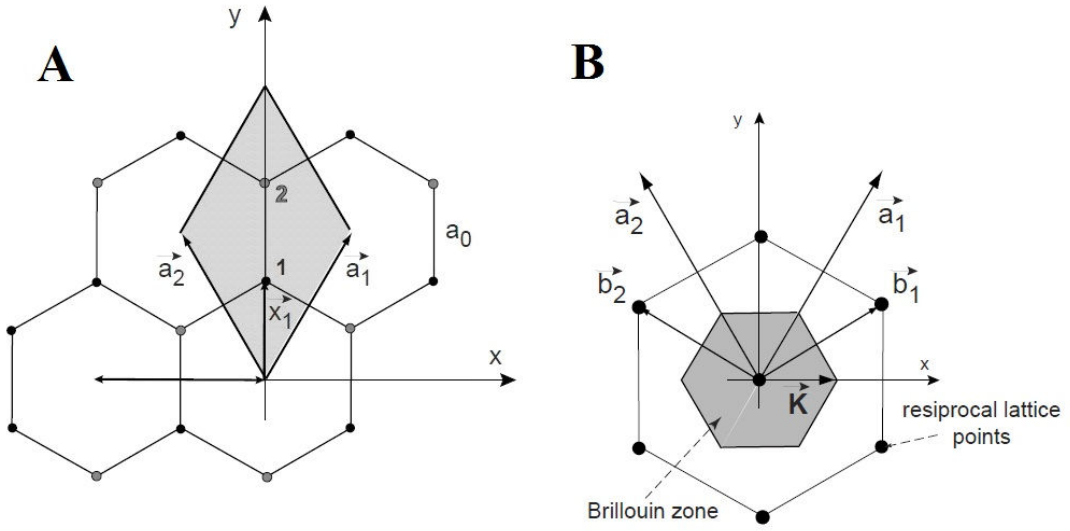

Figure 1.1 Honeycomb structure of graphene.
(A) Real space lattice showing lattice vectors $\mathbf{a}_1$ and $\mathbf{a}_2$ and the unit cell (shaded area).
(B) Momentum space showing first Brillouin zone (shaded area).

In the tight-binding model, which is closely related to linear combination of atomic orbitals (LCAO), a Bloch wavefunction is employed as:

$$\Psi_k = \sum_{R \in G} e^{ikR} \phi(x - R), \tag{1.1}$$

where G is the set of all lattice vectors and $\boldsymbol{k}$ is any allowed wave vector. $\phi(\boldsymbol{x}\text{-}\boldsymbol{R})$ is the wavefunction of the unit cell at position $\boldsymbol{R}$. In LCAO approximation, $\phi(\boldsymbol{x}\text{-}\boldsymbol{R})$ is a linear combination of the two atomic wavefunctions located at position 1 and 2 in the unit cell:

$$\phi(x - R) = \chi_1 \phi_1(x) + \chi_2 \phi_2(x) \tag{1.2}$$

With the wavefunction of the carbon atom p_z state φ(x) and vector x_1 defined in Figure 1.1A, $\phi_1(x)$ and $\phi_2(x)$ can be written out explicitly as:

$$\begin{aligned} \phi_1(x) &= \varphi(x - R - x_1) \\ \phi_2(x) &= \varphi(x - R - 2x_1) \end{aligned} \tag{1.3}$$

Let $h(x)$ be the Hamiltonian of carbon atoms.

$$h(x)\varphi(x) = \varepsilon\varphi(x) \ , \tag{1.4}$$

where ε is the energy of the p_z states and

$$h(x) = \frac{p^2}{2m} + V(x) \tag{1.5}$$

The total potential in graphene is the summation of the atomic potentials of all the carbon atoms. The Hamiltonian for a single electron is

$$H(x) = \frac{p^2}{2m} + \sum_{R\in G}\left[V(x-R-x_1) + V(x-R-2x_1)\right] \tag{1.6}$$

with the Schrodinger equation

$$H(x)\Psi_k(x) = E(k)\Psi_k(x). \tag{1.7}$$

By applying *H(x)* to $\phi_1(x)$ at unit cell ***R***,

$$H(x)\phi_1(x) = \left[\frac{p^2}{2m} + V(x-R-x_1) + V(x-R-2x_1)\right]\phi_1(x) + \sum_{R'\neq R}\left[V(x-R'-x_1) + V(x-R'-2x_1)\right]\phi_1(x)$$

$$= \left[\frac{p^2}{2m} + V(x-R-x_1)\right]\phi_1(x) + V(x-R-2x_1)\phi_1(x) + \sum_{R'\neq R}\left[V(x-R'-x_1) + V(x-R'-2x_1)\right]\phi_1(x)$$

With equation (1.3)-(1.5), the equation above becomes:

$$H(x)\phi_1(x) = \varepsilon\phi_1(x) + \left\{V(x-R-2x_1) + \sum_{R'\neq R}\left[V(x-R'-x_1) + V(x-R'-2x_1)\right]\right\}\phi_1(x) \tag{1.8}$$

The energy of p_z states can be defined as zero in graphene. Equation (1.8) further simplifies to

$$H(x)\phi_1(x) = \left\{V(x-R-2x_1) + \sum_{R'\neq R}\left[V(x-R'-x_1) + V(x-R'-2x_1)\right]\right\}\phi_1(x) \tag{1.9}$$

Similar to $\phi_2(x)$ at unit cell ***R***,

$$H(x)\phi_2(x) = \left\{V(x-R-x_1) + \sum_{R'\neq R}\left[V(x-R'-x_1) + V(x-R'-2x_1)\right]\right\}\phi_2(x) \quad (1.10)$$

With equation (1.1), (1.2), (1.9) and (1.10),

$$\begin{aligned} H(x)\Psi_k(x) &= \sum_{R\in G} e^{ikR}\left[\chi_1 H\phi_1(x) + \chi_2 H\phi_2(x)\right] \\ &= \sum_{R\in G} e^{ikR}\left\{V(x-R-2x_1) + \sum_{R'\neq R}\left[V(x-R'-x_1) + V(x-R'-2x_1)\right]\right\}\phi_1(x)\chi_1 \quad (1.11) \\ &+ \sum_{R\in G} e^{ikR}\left\{V(x-R-x_1) + \sum_{R'\neq R}\left[V(x-R'-x_1) + V(x-R'-2x_1)\right]\right\}\phi_2(x)\chi_2 \end{aligned}$$

The wavefunction of carbon atom 1 at unit cell $\boldsymbol{R}$ = 0 can be defined as $\phi_1^0(x) = \varphi(x-x_1)$. In order to evaluate $\left\langle \phi_1^0 \middle| H \middle| \Psi_k \right\rangle$, we need to set up two rules in nearest-neighbor approximation. First, the overlap of two wavefunctions is ignored if the distance between them is longer than the length of σ bond. For example, most of the terms associated with parameter χ_1 in equation (1.11) do not pass the first rule except the terms with $\boldsymbol{R}$ = 0, e. g., $\left\langle \phi_1^0 \middle| V(x-2x_1) \middle| \phi_1^0 \right\rangle$. Second, the potential coupling the two wavefunctions must be the atomic potential of one of the wavefunctions. $\left\langle \phi_1^0 \middle| V(x-2x_1) \middle| \phi_1^0 \right\rangle$ can not pass the second rule. (It is essentially an average of atom 2's potential weighted by probability of atom 1's p_z electron.)

$\left\langle \phi_1^0 \middle| H \middle| \Psi_k \right\rangle = (\left\langle \phi_1^0 \middle| V(x-x_1) \middle| \phi_2^0 \right\rangle + e^{ik(-a_1)}\left\langle \phi_1^0 \middle| V(x-x_1) \middle| \phi_2^{-a_1} \right\rangle + e^{ik(-a_2)}\left\langle \phi_1^0 \middle| V(x-x_1) \middle| \phi_2^{-a_2} \right\rangle)\chi_2$

Every coupling term here means atom 1 is coupled by its own atomic potential with its nearest neighbor. Because p_z orbital has the rotation symmetry around the z-axis, all the coupling terms are equal and we can use the abbreviation $\left\langle \phi_1^0 \middle| V \middle| \phi_2^0 \right\rangle$. The equation above is simplified as:

$$\left\langle \phi_1^0 \middle| H \middle| \Psi_k \right\rangle = \left(1 + e^{ik(-a_1)} + e^{ik(-a_2)}\right)\left\langle \phi_1^0 \middle| V \middle| \phi_2^0 \right\rangle\chi_2 \quad (1.12)$$

Since the three χ_2 terms are dominant, other smaller terms can be included in the potential V in equation (1.12) as:

$$\left\langle \phi_1^0 \middle| H \middle| \Psi_k \right\rangle = \sum_{R=0,-a_1,-a_2} e^{ikR} \left\langle \phi_1^0 \middle| \left\{ V(x-R-x_1) + \sum_{R' \neq R} \left[V(x-R'-x_1) + V(x-R'-2x_1) \right] \right\} \middle| \phi_2^R \right\rangle \chi_2$$

$$= \chi_2 \sum_{R=0,-a_1,-a_2} e^{ikR} \left\{ \left\langle \phi_1^0 \middle| \sum_{R' \in G} \left[V(x-R'-x_1) + V(x-R'-2x_1) \right] \middle| \phi_2^R \right\rangle - \left\langle \phi_1^0 \middle| V(x-R-2x_1) \middle| \phi_2^R \right\rangle \right\}$$

Again, by symmetry argument the terms in the brackets are the same for different ***R***'s. The equation can be simplified as:

$$\left\langle \phi_1^0 \middle| H \middle| \Psi_k \right\rangle = \alpha(k) \gamma_1 \chi_2 , \tag{1.13}$$

where

$$\alpha(k) = 1 + e^{ik(-a_1)} + e^{ik(-a_2)} \tag{1.14}$$

and

$$\gamma_1 = \left\langle \phi_1^0 \middle| \sum_{R' \in G} \left[V(x-R'-x_1) + V(x-R'-2x_1) \right] \middle| \phi_2^0 \right\rangle - \left\langle \phi_1^0 \middle| V(x-2x_1) \middle| \phi_2^0 \right\rangle \tag{1.15}$$

Similar to equation (1.13),

$$\left\langle \phi_2^0 \middle| H \middle| \Psi_k \right\rangle = \alpha^*(k) \gamma_1 \chi_1 \tag{1.15}$$

Utilizing equation (1.7), (1.13) and (1.15) and keeping only the onsite term in $\left\langle \phi \middle| \Psi_k \right\rangle$, we have the tight-binding equations.

$$\begin{aligned} \alpha(k) \gamma_1 \chi_2 &= E(k) \chi_1 \\ \alpha^*(k) \gamma_1 \chi_1 &= E(k) \chi_2 \end{aligned} \tag{1.16}$$

In matrix form,

$$\begin{pmatrix} E(k) & -\alpha(k)\gamma_1 \\ -\alpha^*(k)\gamma_1 & E(k) \end{pmatrix} \begin{pmatrix} \chi_1 \\ \chi_2 \end{pmatrix} = 0 \tag{1.17}$$

Solving the equation, we obtain the energy of the π bands.

$$E(k) = \pm\gamma_1 \left|\alpha(k)\right| \tag{1.18}$$

With equation (1.14), the explicit form the energy is

$$E(k) = \pm\gamma_1 \sqrt{3 + 2\cos(k \cdot a_1) + 2\cos(k \cdot a_2) + 2\cos(k \cdot (a_2 - a_1))}\,, \tag{1.19}$$

or alternatively

$$E(k) = \pm\gamma_1 \sqrt{1 + 4\cos\left(\frac{\sqrt{3}ak_y}{2}\right)\cos\left(\frac{ak_x}{2}\right) + 4\cos^2\left(\frac{ak_x}{2}\right)}, \tag{1.20}$$

where $a = \sqrt{3}a_0$ is the lattice constant.

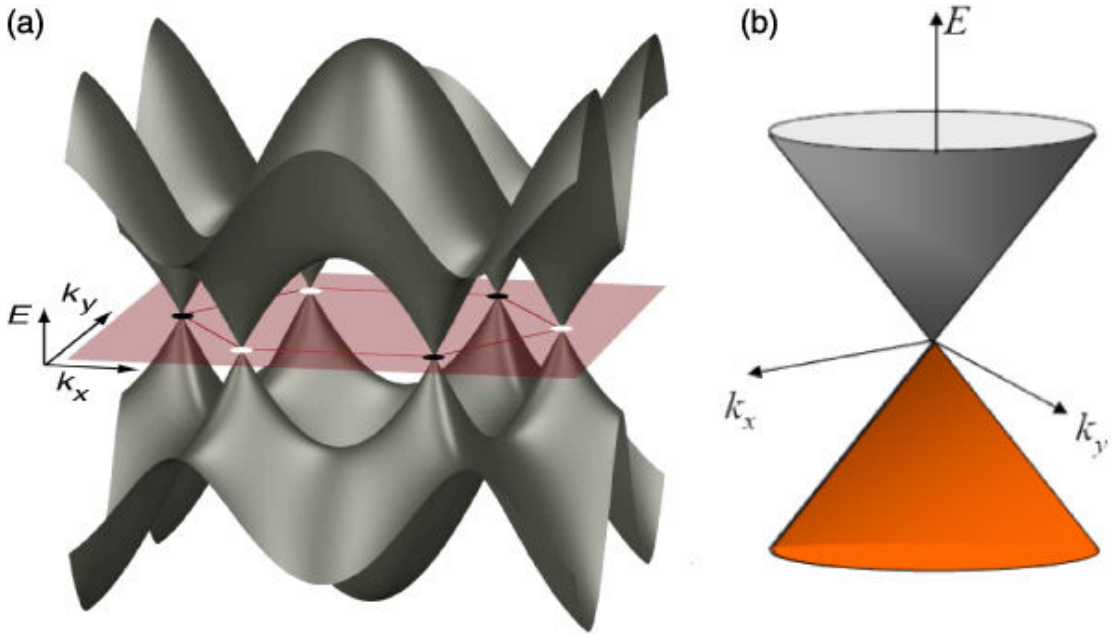

Figure 1.2 Graphene band structure.
(a) π bands (b) One of the Dirac cone (from Ref. [11])

The π bands are plotted in Figure 1.2. At $E(k) = 0$, they are touching at the corners of the first Brillouin zone, e.g., **K** point in Figure 1.1B. Note that **K** + $\mathbf{b_1}$ and **K** - $\mathbf{b_2}$ corners are equivalent points to **K** in first Brillouin zone, since they are only different by a reciprocal lattice vector. All the three corners (white spots in Figure 1.1a) are called

K points and the other three corners (spots in Figure 1.1b) are called **K'** points. At each **k** point there are 8 energy levels (6 σ-band levels and 2 π-band levels) and in each unit cell there are 8 electrons. Because of the spin degeneracy, only 4 energy levels are filled. Therefore, the Fermi energy $E_F = 0$ and Fermi surface is the points where the π bands touch each other. Expanding equation (1.19) or (1.20) near **K** and **K'**, we find that the dispersion relations are linear near the Fermi surface (Figure 1.2).

Another way to examine the dispersion relation is to expand **k** in equation (1.17). Near $K = \frac{b_1 - b_2}{3}$, we use the form **k = K + κ**, where **κ** is a small vector. The phase factor in equation (1.14) is expanded as:

$$\begin{aligned} \alpha &= 1 + e^{-i\frac{2\pi}{3}} e^{-i\kappa a_1} + e^{i\frac{2\pi}{3}} e^{-i\kappa a_2} \\ &= 1 + (-\frac{1}{2} + i\frac{\sqrt{3}}{2})(1 - i\kappa a_1) + (-\frac{1}{2} - i\frac{\sqrt{3}}{2})(1 - i\kappa a_2) \\ &= \frac{3}{2} a_0 \left(\kappa_x + i\kappa_y\right) \end{aligned} \tag{1.21}$$

Together with the energy $E(k) = E(K) + \varepsilon(\kappa)$, the tight binding equation (1.17) becomes

$$\begin{pmatrix} \varepsilon(\kappa) & \gamma_1 \frac{3a_0}{2}\left(\kappa_x + i\kappa_y\right) \\ \gamma_1 \frac{3a_0}{2}\left(\kappa_x - i\kappa_y\right) & \varepsilon(\kappa) \end{pmatrix} \begin{pmatrix} \chi_1 \\ \chi_2 \end{pmatrix} = 0 \tag{1.22}$$

If we define $v_F = \frac{3a_0\gamma_1}{2\hbar}$, equation (1.22) takes an interesting form:

$$-v_F\left(p_x\sigma_x + p_y\sigma_y\right)\begin{pmatrix} \chi_1 \\ \chi_2 \end{pmatrix} = \varepsilon\begin{pmatrix} \chi_1 \\ \chi_2 \end{pmatrix}, \tag{1.23}$$

where $p = \hbar\kappa$ and σ_x and σ_y are Pauli matrices, which do not operate on the real spinor, but on the two component wavefunction of Equation (1.2). Thus, the matrix $\begin{pmatrix} \chi_1 \\ \chi_2 \end{pmatrix}$ is called the "pseudospin".

At K' the expansion has a similar result, they both have the linear dispersion relation

$$\varepsilon(p) = \pm v_F |p| \ . \tag{1.24}$$

The Lagrangian of a Dirac fermion in (2+1)-dimensions can take the form:

$$L = \overline{\psi}\left(i\gamma^\mu \partial_\mu - m\right)\psi \ , \tag{1.25}$$

where $\gamma^\mu = \left(\sigma^3, i\sigma^1, i\sigma^2\right)$[3]. When *m*=0, it is obvious that equation (1.23) and (1.25) represent the same mathematical expression. In other words, the two-component Schrodinger equation of graphene in tight-binding model is the simulation of massless Dirac fermions in 2D (spatial dimensions).

The simulation is not trivial. The carriers in graphene behave like massless Dirac fermions, which creates new physics in graphene and few-layer graphene thin films, e.g., high electron mobility[12], high opacity[13], the anomalous quantum Hall effect[9, 10], and Klein tunneling[14]. In addition to the unique carriers, the strong sp^2 bonds in graphene and the atomic thickness make graphene a special 2D material with many extraordinary mechanical, electrical and optical properties, such as high thermal conductivity[15], strong electric field effect[4], extreme surface sensitivity[16].

The rediscovery of graphene in 2004 is a great unexpectation. Since then, graphene has become a major focus of condensed matter physics research. Besides the tremendous interest in academic research, various suggestions have been made for the

potential applications of graphene, e. g., fast analog transistors[4], high-performance ultracapacitors[17], sensitive photon detectors[18] and tunable plasmonic metamaterials[19]. One example is the prototype touch screen using graphene as a transparent conductive thin film[20], which demonstrates the exciting future of this novel material. For review of recent developments in graphene science and technology, see references [21] and [22].

This thesis is focused on two topics: the scattering of charge carriers by charged impurities on the surface of bilayer graphene, and exploiting the surface sensitivity of graphene thin films to study adsorbed species. The electronic transport theory of graphene and its bilayer is introduced in Chapter 2, where charged impurity scattering and short-range scattering are discussed in semi-classical Boltzmann transport theories. The experimental methods, including device fabrication and experimental setup, are presented in details in Chapter 3. Chapter 4 discusses the first experiments to directly probe the effects of varying charged impurity density and dielectric background in bilayer graphene. Chapter 5 is devoted to the coadsorption of water and dilute potassium. A strong dielectric screening effect within the hydration shells of potassium ions has been observed and the radius of the hydration region is estimated with Boltzmann theories. Chapter 6 covers a novel experimental method, which combines graphene electronic transport measurements with surface adsorption and temperature-programmed desorption in UHV. The electronic signals from graphene devices are interpreted as the impact of surface phenomena such as chemical reactions, phase changes, and desorption. The thesis is summarized in Chapter 7 with the outlook for future work.

Chapter 2 Transport theories of graphene and its bilayer

In the "Scotch tape" method, graphene is transferred to 300 nm thick SiO_2 on Si substrate in order to increase the optical contrast of the atomically thin film. In the early stage of graphene research, most graphene devices were conveniently fabricated on Si/SiO_2 substrate, with SiO_2 as the dielectric material and heavily doped Si as back gate. Common features were observed in their transport properties. When conductivity σ was measured at different gate voltages V_g, σ is a linear function of V_g, i.e. $\sigma \sim |V_g - V_{g,min}|$, except near $V_{g,min}$, the gate voltage at which the conductivity is a minimum σ_{min}. A typical measurement of $\sigma(V_g)$ for graphene on SiO_2/Si is shown in Figure 2.1.

V_g changes the carrier density n in graphene devices, with $n = (c_g/e)(V_g - V_{g,min})$, where c_g is the gate capacitance per unit area, approximately 1.1×10^{-4} F/m^2 for the 300 nm SiO_2 gate dielectric. At $V_{g,min}$ the carrier density should be zero and the Fermi surface should lie right at the Dirac points, with a vanishing density of states. Contrary to intuition, σ does not vanish at $V_{g,min}$, but has a finite value σ_{min}.

In this chapter, semi-classical Boltzmann transport theories are introduced to explain the linear dependence of conductivity on carrier density and the existence of the finite minimum conductivity within the context of graphene with disorder modeled by a random Coulomb potential representing charged impurities.

2.1 Transport theory of single-layer graphene

Charged impurity scattering has been widely studied in 2D electron systems (2DESs) especially in the context of understanding the transport properties of MOSFETs[23-25]. Although graphene has massless Dirac fermions as its charge carriers,

the charge carriers in graphene can still be scattered by the Coulomb potential of charged impurities as in MOSFETs and the charged impurity scattering is dominant at low carrier density.

For single layer graphene, in Boltzmann transport theory the semi-classical diffusive conductivity[26] is given by

$$\sigma = \frac{g_s g_v e^2}{h} \frac{E_F \tau}{2\hbar}, \tag{2.1}$$

where $g_s = g_v = 2$ are the spin and valley degeneracy factors and the scattering time τ at temperature $T = 0$ is given by

$$\frac{\hbar}{\tau(k)} = \frac{n_{imp}}{4\pi} \int dk' \left[\frac{V(|k-k'|)}{\varepsilon(|k-k'|)} \right]^2 \left[1 - \cos^2(\theta)\right] \delta(E_k - E_{k'}), \tag{2.2}$$

where n_{imp} is the two-dimensional density of charged impurities and $V(q) = 2\pi e^{-qd} e^2 / (\kappa q)$ is the Fourier transform of bare Coulomb potential at the transfer momentum q:

$$q = |k - k'| = 2k_F \sin(\theta/2), \tag{2.3}$$

where d is the impurity-graphene distance (assumed to be ~ 1 nm for impurities near the SiO_2 surface) and κ is the effective dielectric constant of the surrounding media. For graphene on SiO_2 with vacuum above, $\kappa \approx 2.5$, taken as the average of dielectric constants of SiO_2 ($\kappa \approx 3.9$) and vacuum ($\kappa = 1$).

Using the function form[27] of $\varepsilon(|k-k'|)$ from the random phase approximation (RPA) to evaluate the integral in Equation 2.2, we get the conductivity

$$\sigma = \frac{20e^2}{h} \frac{n}{n_{imp}}, \tag{2.4}$$

where n is the carrier density. This result explains the linear dependence of conductivity on carrier density at high carrier density.

However, near the minimum conductivity carrier density is too low for this treatment to be accurate. The corresponding Fermi surface can not cover the potential fluctuations generated by the charged impurities. Charged impurities not only scatter the carriers, but create fluctuations in carrier density that are larger than the average carrier density ("electron and hole puddles") across a macroscopic graphene sample. Equation 2.4 is still valid at low carrier density, but the carrier density must be determined self-consistently from the screening of the charged impurities by the carriers they induce.

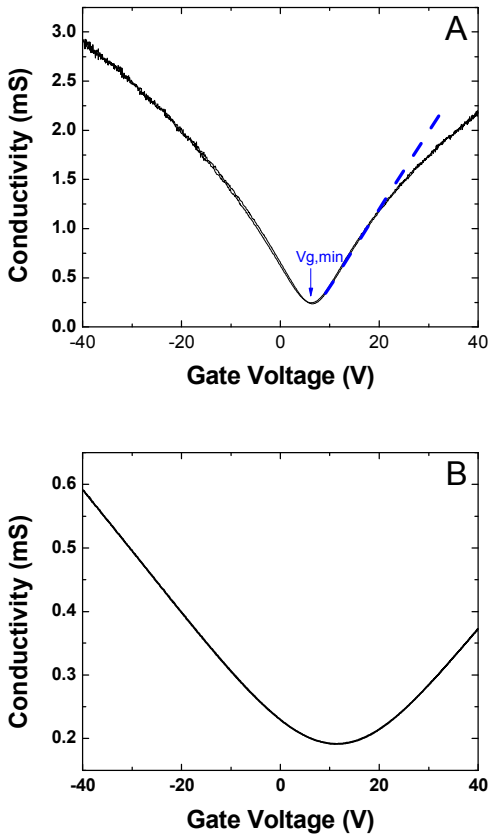

Figure 2.1 Gate voltage dependence of conductivity.
(A) Single layer graphene (B) Bilayer graphene

A self-consistent theory is used to evaluate the screened voltage fluctuations induced by charged impurities. The residue carrier density n^* can be calculated from a self-consistent equation:

$$\frac{n^*}{n_{imp}} = f(n^*), \tag{2.5}$$

where n_{imp} is the density of charged impurities and the exact function form of $f(n^*)$ is available in Ref.[26]. For charged impurities of a single sign, the minimum conductivity occurs at a carrier density $\overline{n}$ added by the gate voltage $V_{\mathrm{g,min}}$ via capacitance density c_g. $\overline{n} = c_g V_{g,\mathrm{min}} / e$ is determined by n^* and n_{imp}:

$$\overline{n} = \frac{n_{imp}^2}{4n^*}. \tag{2.6}$$

From Equation 2.5 and 2.6, $\overline{n}$ has an approximate power law dependence with n_{imp} due to the function $f(n^*)$. Therefore, in experimental data $V_{g,\mathrm{min}} \propto n_{imp}^b$ with b = 1.2-1.3.

The approximate width of the minimum conductivity region in gate voltage is given by $\Delta V_{\mathrm{g}} = 2n^*e/c_{\mathrm{g}}$, which increases with n_{imp}. If $n < n^*$, the carrier density used in Equation 2.4 is approximated by n^*. If $n > n^*$, conductivity takes the linear form in Equation 2.4. Together,

$$\sigma(n) = \begin{cases} \dfrac{20e^2}{h}\dfrac{n^*}{n_{imp}} & if \quad n < n^* \\ \dfrac{20e^2}{h}\dfrac{n}{n_{imp}} & if \quad n > n^* \end{cases} \tag{2.6}$$

The mobility of single layer graphene $\mu = \sigma/(ne)$. From the linear part of Equation 2.6,

$$\mu = \frac{20e}{h}\frac{1}{n_{imp}}. \tag{2.7}$$

For clean samples the charged impurity scattering is weak at high carrier density (In Equation 2.6, σ(n) is large with small n_{imp} and large n). Although charged impurity scattering is dominant over a wide range of gate voltage, at high gate voltage the n-independent short-range scattering[28], in addition to charged impurity scattering, is needed to explain the deviation from the linear behavior in clean samples (see Figure 2.1A). Physically, the short-range scattering can come from point defects or dislocations in carbon lattice.

The difference between short-range scattering and Coulomb scattering can be easily explained by Boltzmann transport theory discussed above. Coulomb potential $V(q) \propto q^{-1}$ and short-range potential is independent of q. The integral in Equation 2.2 is proportional to k_F^{-1} and k_F, respectively, for Coulomb potential and short-range potential. With $E_F \propto k_F$, conductivity $\sigma \propto k_F^2 \propto n$ for Coulomb potential and σ is independent of n for short-range scattering. Therefore the experimentally observed sublinear σ(n) can naturally be explained by a combination of long-range ($\sigma \propto n$) and short-range ($\sigma \propto$ constant) scattering, since the conductivities add in inverse according to Matthiessen's rule. However, a recent experiment[29] provides an alternative explanation that correlations in long-range scatters can explain the sublinearity in σ(n) without invoking point disorder.

2.2 Transport theory of bilayer graphene

The tight binding calculation for bilayer graphene can be expanded near the Fermi surface. An effective Hamiltonian[30] at low energies may be written

$$H = -\frac{1}{2m}\begin{pmatrix} 0 & (p_x - ip_y)^2 \\ (p_x + ip_y)^2 & 0 \end{pmatrix}, \tag{2.8}$$

where $m \approx 0.033 m_e$, calculated from the in-plane coupling and out-of-plane coupling parameters. In contrast to single-layer graphene, bilayer graphene has a massive dispersion, but is still gapless, with conduction and valence bands touching at the K points (see Figure 2.2).

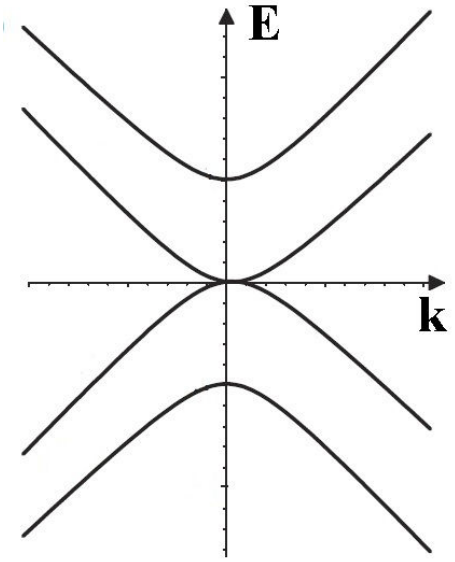

Figure 2.2 Low-energy band structure of bilayer graphene

From Equation 2.8 charged impurity scattering can be calculated self-consistently in Boltzmann transport theory[31]. Making the simplifying assumption that screening is complete within the Thomas-Fermi approximation (i.e. the screening wavevector is much greater than the Fermi wavevector), one arrives at the result:

$$\sigma(n) = \begin{cases} \dfrac{4e^2}{\pi h}\sqrt{\dfrac{\tilde{n}}{n_{imp}}} & if \quad n < n^* \\ \dfrac{4e^2}{\pi h}\dfrac{n}{n_{imp}} & if \quad n > n^* \end{cases}, \tag{2.9}$$

where $\tilde{n} \approx 140 \times 10^{10}\, cm^{-2}$ and residue carrier density $n^* = \sqrt{n_{imp}\tilde{n}}$. In bilayer graphene the $V_{g,min}$-added carrier density $\bar{n} = n_{imp}$. This result is revisited and refined in Chapter 4.

However, in contrast to single-layer graphene where short-range scattering gives a carrier-density-independent conductivity (see Table 2.1), the conductivity of bilayer graphene with short-range scattering also has a linear dependence on n, which can explain the linear behavior in bilayer graphene as well (see discussion in Chapter 4). Therefore the dependence of conductivity on carrier density alone cannot determine the dominant scattering mechanism in bilayer graphene.

	2DEG	Graphene	Bilayer
Bare Coulomb scattering	$\sigma \sim n^2$	$\sigma \sim n$	$\sigma \sim n^2$
Screened Coulomb	$\sigma \sim n$	$\sigma \sim n$	$\sigma \sim n$
Short-range scattering	$\sigma \sim n$	$\sigma \sim$ const	$\sigma \sim n$

Table 2.1 Summary of Boltzmann transport results in two-dimensional electron gas (2DEG), single layer graphene and bilayer graphene. Taken from Ref. [31]

Chapter 3 Experimental methods

This chapter summarizes the device fabrication and experimental setup of the experimental work in the following chapters. The device fabrication section includes mechanical exfoliation, optical identification of graphene, Raman characterization, field effect transistor (FET) device fabrication and annealing. The experimental setup discussion is divided into 4 sections: ac lock-in technique, Helitran UHV compatible LT-3B open cycle cryostat, adsorption in UHV and temperature programmed desorption (TPD).

3.1 Graphene device fabrication

In this work, graphene thin films have been mechanically exfoliated[32] from bulk graphite (Kish graphite or natural graphite). I used two types of techniques (Technique 1 and Technique 2, whose details have been constantly changing from time to time) in the experiments of this thesis.

Technique 1 follows the standard "Scotch tape" method[32], i.e., exfoliating bulk graphite between tapes. Multiple exfoliations are usually needed to cover the tapes with thin layers of freshly exposed graphite crystal, which are then pressed onto SiO_2 on Si substrates to transfer graphene by micro-mechanical exfoliations.

In Technique 2, tapes are only used to cleave the bulk graphite to expose the perfect graphite crystal inside graphite samples. Fine-tipped tweezers are employed to pick up thin graphite films that are loosely attached to the fresh graphite surface. These thin films are placed on SiO_2/Si substrates and are pressed down with clean glass slides to make the bottom graphene layers fully interact with the substrates. After this, the top

layers are scratched off by sharp and clean edges, e.g., edges of glass slides, and single layer graphene can be left on the substrate.

After the transfer step in Technique 1 or the scratch step in Technique 2, SiO_2/Si substrates are examined under optical microscopes. The 300nm-thick SiO_2 enhances the interference of visible light and provides good optical contrast for graphene thin film on it (a typical optical micrograph is shown in Figure 3.1). The optical contrast can be calibrated for different layer numbers of graphene thin film. Single layer graphene corresponds to the weakest contrast. Bilayer contrast can be identified from overlapping single layer graphene. For single layer and bilayer graphene, after optical identification, their crystalline structures need to be further confirmed by Raman spectra.

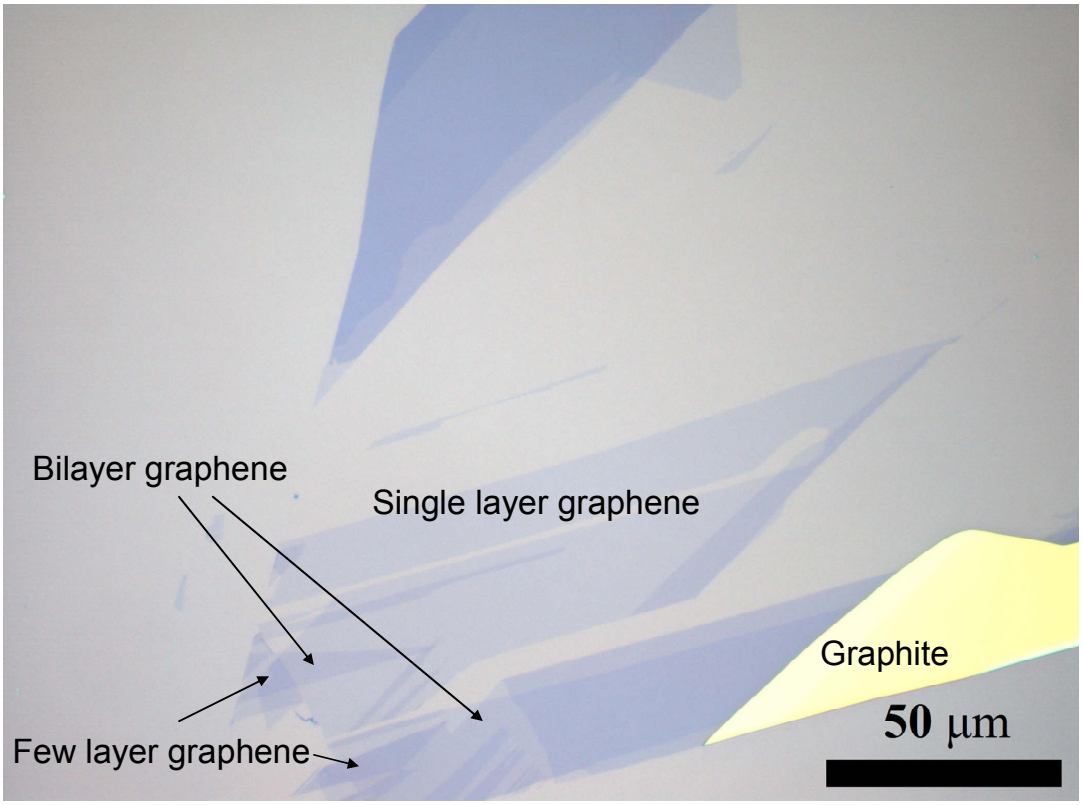

Figure 3.1 Optical image of graphene on SiO_2/Si substrate.

A typical Raman spectrum of graphene (see Figure 3.2) has two major peaks: the G peak at about 1580 cm^{-1} results from in-plane vibration of sp^2-bonded carbon atoms, and the 2D (sometimes called G') peak at about 2650 cm^{-1} is the second-order overtone of the D band (breathing modes of carbon rings)[33, 34]. The G and 2D peaks are enhanced by a resonant Raman process, but the D peak is only resonantly enhanced in the presence of intervalley scattering caused by point defects (hence the name "D" for defect)[33, 34]. Single layer graphene has a single Lorentzian 2D peak shape (Figure 3.2A) while bilayer graphene's 2D peak (Figure 3.2B) consists of 4 Lorentzian components due to the splitting of the band structure in Bernal-stacked bilayer graphene, and therefore acts as a fingerprint to identify such bilayers[35]. The Raman data in this thesis were taken at a HORIBA LabRAM HR-VIS micro-Raman system. The Raman spectra provide more information than identification of single layer and bilayer graphene. The D peak characterizes the level of defects in graphene, which is very low in graphene exfoliated from high quality graphite. The small G to 2D peak ratio distinguishes single layer graphene from multilayer turbostratic graphene[36] with similar 2D peak.

After Raman identification, electrical contacts are made to graphene by electron-beam lithography as follows. Substrates with graphene samples are spin-coated with two-layer e-beam resist, which consists of a bottom layer of MMA/MAA copolymer (MMA EL11, MicroChem Corp.) spun at 4000rpm for 45 seconds and a top layer of poly(methyl methacrylate) resist (950 PMMA A4, MicroChem Corp.) spun at 6000 rpm for 45 seconds. In order to align lithography patterns with graphene samples, first the relative position of each graphene thin film is roughly measured relative to some large features (a corner of the substrate or a cross written by electron-beam lithography) using

the optical microscope. The sample is inserted into a scanning electron microscope (SEM; FEI XL30). Based on the relative position and the large feature visible under SEM, the substrate is moved by the SEM mechanical stage such that the graphene thin film is near the center of the electron-beam scanning area. A pattern of alignment markers is written around the graphene sample using the Nanometer Pattern Generation System (NPGS) software control. The sample is then removed from the SEM and the resist is developed. 30-50 nm of Cr/Au metal is deposited as alignment markers. Imaging again in the optical microscope is performed to provide precise positioning information of the graphene relative to the alignment markers.

With all the rough and precise positioning information and the alignment markers, the sample is again inserted into the SEM for patterning of the desired metal electrode pattern to contact the graphene. The resist is developed in PMMA and copolymer resist developer (IPA/MIBK 3:1, MicroChem Corp.) for 40 seconds. Metal electrodes are deposited by thermal evaporation. Typically the electrodes consist of 5nm of Cr adhesion layer followed by 50nm of Au. Liftoff is accomplished by immersing substrates in acetone for 2 hours.

Graphene devices are etched into regular geometry (see Figure 3.3) by oxygen plasma in reactive ion etching systems. Etch masks are prepared by similar electron-beam lithography and resist developing techniques in the previous paragraphs except that only PMMA is used as the resist to achieve better resolution. Details on the device geometry and electrical measurement are discussed in section 3.2.1.

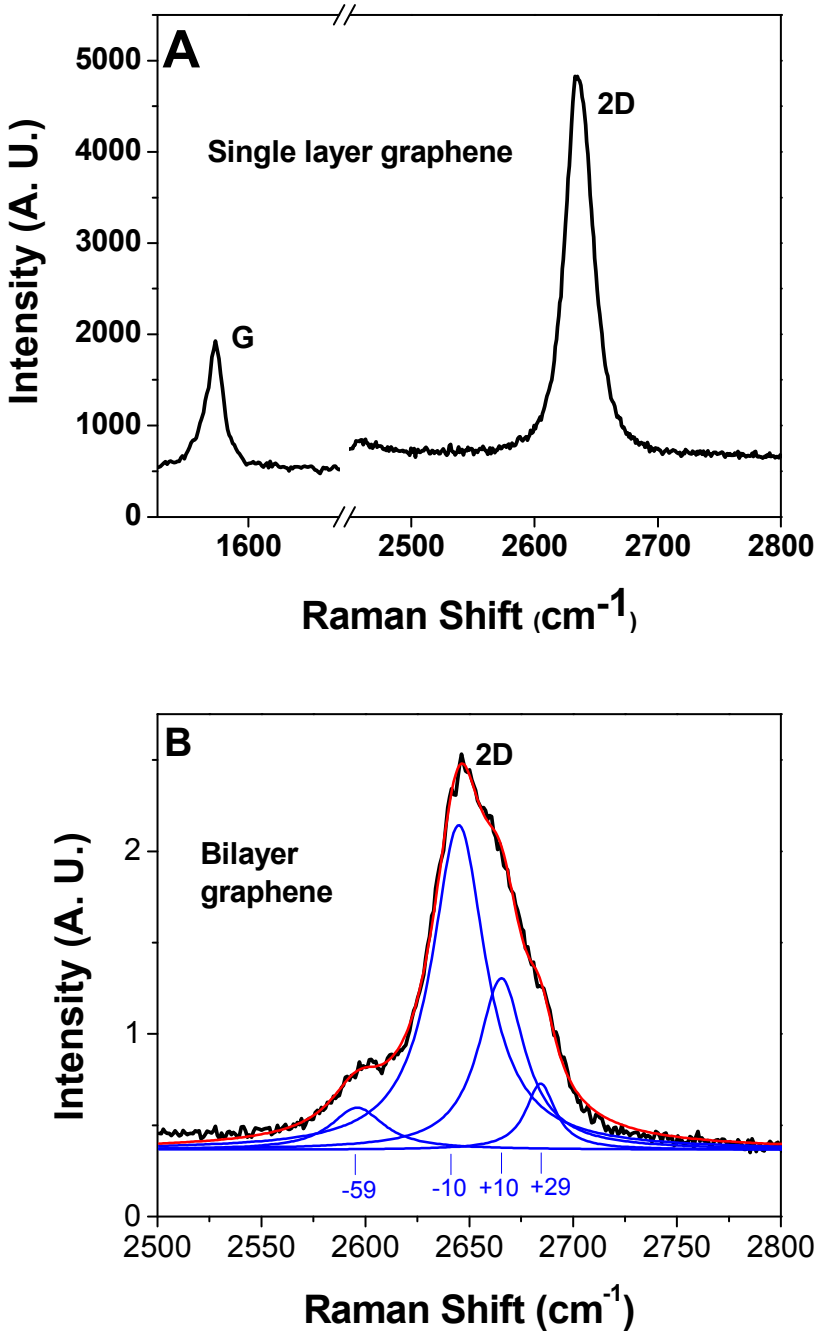

Figure 3.2 Raman spectra with 633nm laser excitation wavelength of (A) single layer graphene and (B) bilayer graphene. Black curves are experimental data. The bilayer 2D peak can be decomposed into four Lorentzian components (blue) whose sum is shown in red.

For UHV experiments, it is necessary to clean the graphene samples of any resist residue to expose the graphene surface. This is accomplished by annealing the samples in a tube furnace under a flow of Ar (1900 ml/min) and H_2 (1700 ml/min) at 350 ºC for 1 hour[37]. AFM topography shows that a 2-3 nm thick resist residue layer is removed by annealing, and previous studies by our group have shown that atomically-clean graphene surfaces may be prepared in this manner[37]. After annealing, it is found that graphene devices are heavily *p*-doped in ambient conditions likely due to oxygen assisted by water vapor in air[38-40]. However, the doping can be easily removed by bakeout in vacuum at above 400K.

3.2 Experimental setup

3.2.1 AC lock-in technique

Graphene's electrical conductivity is measured by an ac setup utilizing a lock-in amplifier. As shown in Figure 3.3, the lock-in amplifier outputs a sinusoid voltage signal at a frequency (~10Hz) which is low compared to any frequency dependence of graphene's conductivity. A 10MΩ resistor is in series with the graphene device. At different gate voltages, the resistance of graphene devices varies from ~100Ω to ~10k Ω, whose contribution to the total resistance is negligible compared to the 10MΩ resistor, therefore at constant output voltage amplitude, the current amplitude in the circuit is a constant. The voltage difference from the voltage probes on graphene is measured using the lock-in differential inputs A and B. In this way, a four-probe resistivity measurement is performed.

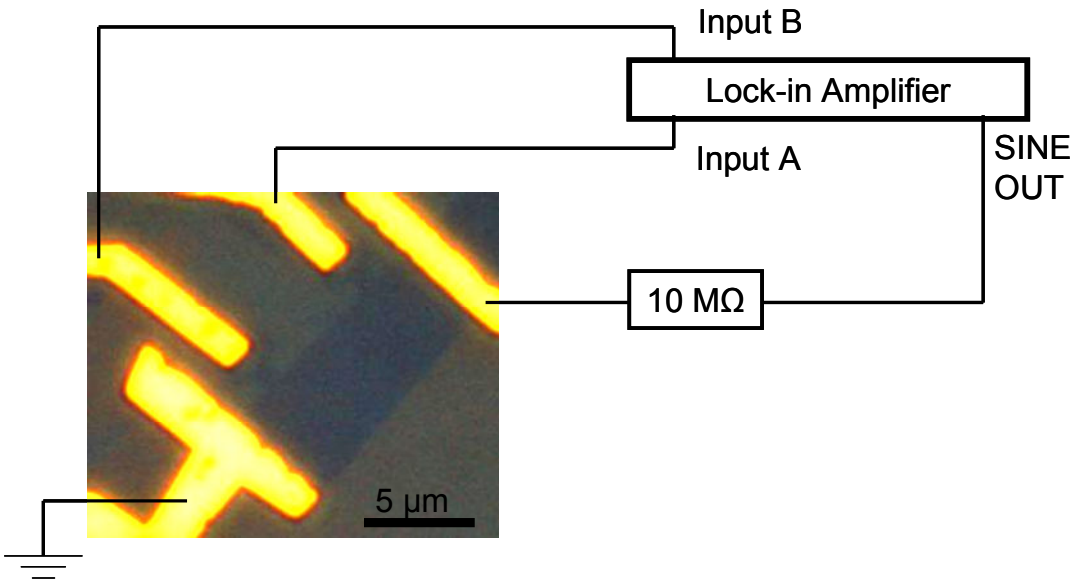

Figure 3.3 Schematic of the ac four-probe measurement.

The graphene devices are etched into a Hall bar-like design for a precise measurement of resistivity (see Figure 3.3). Narrow graphene channels (less than 1 μm) connect the voltage probes to the bulk of the graphene between source and drain electrodes. This ensures that little current flows through the metal voltage probes, and defines a precise aspect ratio of the bulk of the graphene. In the design of graphene devices, some graphene is left around the voltage-probe electrodes to make the graphene-metal junction less vulnerable to electrical shocks.

The lock-in time constant is set at 30 ms, which requires at least a delay of 0.15 s for each data sampling point. At this time constant, the low-pass filter has a cutoff frequency at 5.3Hz, which is lower than the ac reference frequency. With the help of the synchronous filters, the noise from the reference/detection frequency can be easily removed.

3.2.2 Helitran UHV compatible LT-3B open cycle cryostat

The electronic transport properties of graphene devices in UHV environment have been measured with a Helitran UHV compatible LT-3B open cycle cryostat at variable temperatures from 10K to 490K. A custom sample stage is added on the cold tip with electrical wires connected to the instruments outside the UHV chamber via multi-pin feed-throughs of the cryostat (see Figure 3.4).

In order to reach base temperature on the cold tip (4 K using liquid helium, 77 K using liquid nitrogen), electrical wires (coated with insulation layer) are tightly wound around the cold finger to minimize heat leak to the sample stage and a nickel plated copper shield is installed on the cold tip to block thermal radiation from the room-temperature environment. A transfer line introduces liquid helium/nitrogen to the copper cold finger outside UHV chamber. The cryostat is cooled by evaporation of liquid and the generated gas is exhausted out of the cryostat through the cold gas path. A gas flow meter can be attached to the gas exhaust line to control the gas flow rate, which optimizes the cooling power of the cryostat. Experienced users may even be able to stabilize the sample temperature at temperatures from base to room temperature by controlling the exhaust gas flow rate.

A heater and a temperature controller are configured to bake samples in UHV at low heating rate. The maximum baking temperature is limited by the stable working temperature of the wire coating material and the Teflon parts of the cryostat system. 420 K is the recommended temperature for overnight baking and 490 K is the maximum temperature that is only allowed for a short period of time.

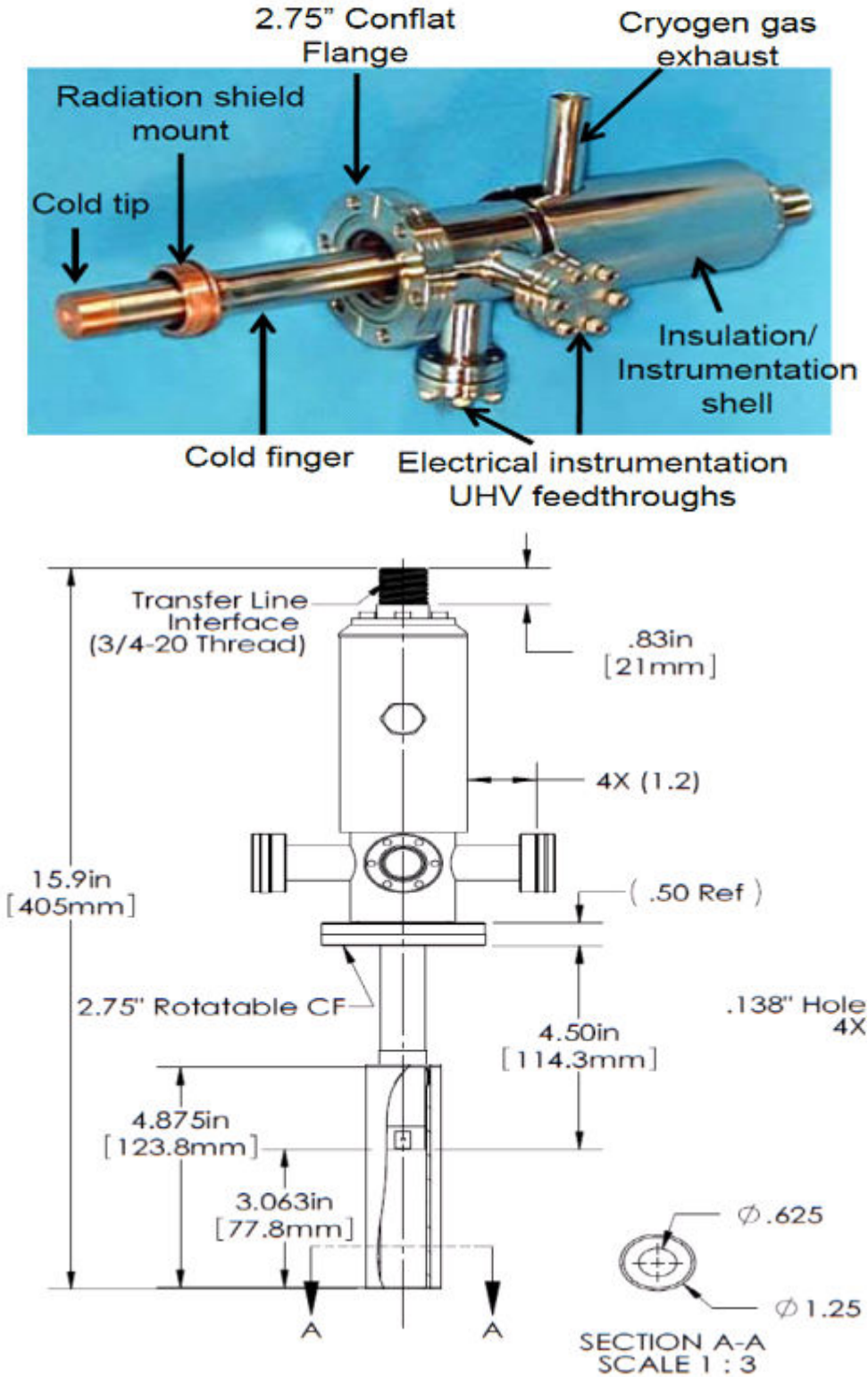

Figure 3.4 LT-3B ultra high vacuum compatible cryostat with dimensions. Electrical wires and custom sample stage not shown. Drawing from Advanced Research Systems, Inc.

In order to perform the rapid heating necessary for thermal desorption experiments (described below in Section 3.2.4) I fabricated a custom high-power Si heater which is inserted between the sample holder and the cold finger. A doped silicon chip is inserted into slots in standard steel electrodes and glued with aluminum oxide paste (from Ceramabond) in a copper envelope, which provides decent thermal conductivity and mechanical properties. This heater is installed under the sample holder and powered by a power supply outside UHV chamber. Thick coated copper wires connect the power supply with the steel electrodes through a UHV compatible feed-through.

Two silicon diodes are attached to the system. One is glued to the cold finger to monitor the cooling power of the liquid helium/nitrogen. The other is installed on the sample holder to measure the device temperature at stable temperature. A third bare-die silicon diode (DT-670E-BR by Lake Shore Cryotronics, Inc.) can be glued right on top of the sample to reflect the real-time temperature during rapid heating/cooling (see Section 3.2.4).

Due to the thermal resistance from the custom sample stage and sample holder, manufacturer's operation base temperature can only be achieved on the cold tip. The sample temperature is usually 10-30 K higher, which depends on the system configuration.

3.2.3 Adsorption in UHV

Graphene samples are usually loaded into the UHV chamber immediately following the H_2/Ar annealing, and further annealed in the UHV environment by overnight baking to expose the graphene surface. The electrically-monitored doping and

mobility of graphene devices are good evidence for the quality and cleanliness of the graphene samples (typically with doping within a few volts near zero gate voltage and mobility above 10,000 $cm^2V^{-1}s^{-1}$).

Adsorbates are deposited on graphene samples by either thermal evaporation using an electrically heated commercial getter as a source, or as gas leaking into the UHV through a calibrated leak valve. The adsorption of potassium and water are described in detail below as two examples to demonstrate these two experimental methods.

In potassium adsorption experiments, a potassium source (SEAS potassium getter) is placed in the UHV chamber facing graphene samples on the cold finger (see Figure 3.5). When a large current (5~7 A) is passed through the getter, potassium is thermally evaporated into the chamber. A shutter is placed between the potassium getter and graphene samples to control the adsorption. During sample bakeout, a current of 2-3 A is used to outgas the getter while the shutter is fixed at off position to avoid any sample contamination. After all preparation, graphene devices are exposed to the *in situ* adsorption of potassium atoms at low temperatures, whose amount is controlled by the "on" time of the shutter. In our experiments, the coverage of adsorbed potassium is on order of 0.01-0.001 of a monolayer, hence a direct measurement of the deposition rate is impractical. The actual amount of potassium deposited is inferred indirectly from the doping of the graphene (see Chapter 4).

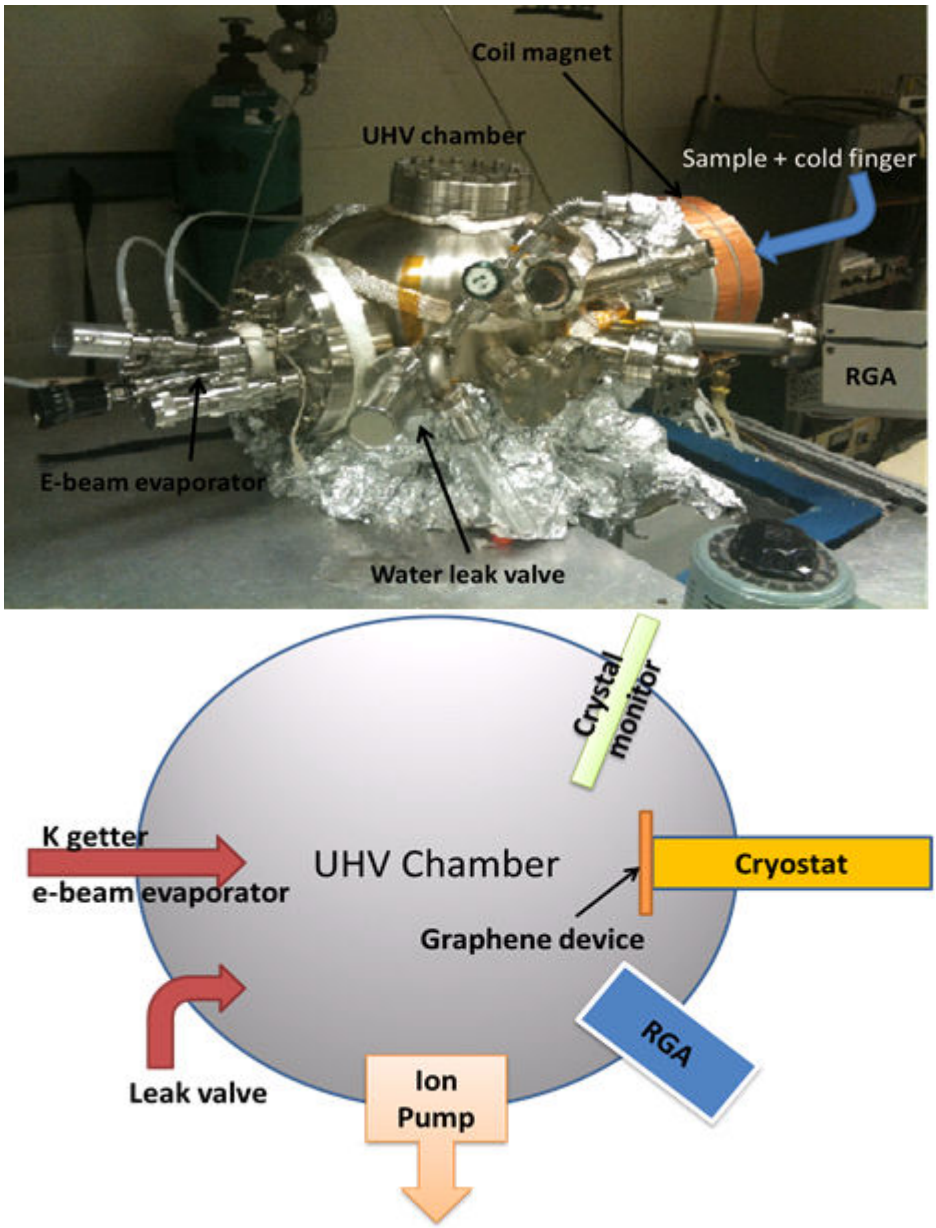

Figure 3.5 UHV chamber: photograph (top) and schematic (bottom)

In ice deposition experiments, a leak valve introduces water vapor in a controlled way. The water attached to the leak valve is purified by multiple freeze-pump-thaw cycles to minimize impurities. Before experiments, the leak valve is calibrated to produce different partial pressures of water in UHV chamber. At low sample temperatures, water

is leaked into the chamber and deposited on graphene samples as well as the surface of the whole cold finger. The thickness of the ice on graphene is calculated from the partial pressure recorded by a residue gas analyzer (RGA) and duration of the leaking using the assumption that the sticking coefficient of the water is unity.

3.2.4 Temperature programmed desorption

I used the temperature programmed desorption method to analyze the activation energy for desorbing species from graphene. The method is described briefly below.

According to the Arrhenius equation, the reaction rate coefficient k has temperature dependence,

$$k = k_o e^{-\frac{Ea}{k_B T}} \tag{3.1}$$

where k_o is a pre-factor and E_a is the activation energy. E_a corresponds to a potential barrier in an elementary reaction.

Desorption is one type of reaction. The desorption rate r is defined as the change of coverage θ:

$$r = -\frac{d\theta}{dt}. \tag{3.2}$$

For a simple desorption process (other complex processes are beyond the scope of this thesis), the probability to desorb equals the reaction rate coefficient k. The desorption rate at coverage θ is

$$r = k\theta. \tag{3.3}$$

In a typical desorption experiment, the desorption rate is measured by the partial pressure of adsorbates in a mass spectrometer while the system is heated from low temperature. At the beginning, since temperature T is low and k is small, the desorption

rate r is low and coverage θ decreases very slowly. At higher T, k increases and r increases. With increasing r, θ decreases more rapidly. At some temperature, θ becomes so low that r begins to decrease despite the increasing k. Hence the rate r shows a peak as a function of temperature. The desorption rate can be observed by a variety of methods (measuring the sample mass, measuring the desorbed species via mass spectrometer, etc.). At peak temperature T_p, $dr/dt = 0$.

In the temperature programmed desorption (TPD) method, also known as the Redhead method[41], temperature T is programmed as a linear function of time t.

$$T = T_o + \beta t \,, \tag{3.4}$$

where β is the heating rate. From equation (3.1)-(3.3),

$$r = k_o e^{-\frac{Ea}{k_B T}} \theta \tag{3.5}$$

Taking time derivative of both sides of Equation (3.5), we have

$$\frac{dr}{dt} = k_o e^{-\frac{Ea}{k_B T}} (\frac{E_a}{k_B}\frac{1}{T^2})(\frac{dT}{dt})\theta + k_o e^{-\frac{Ea}{k_B T}} \frac{d\theta}{dt} \,. \tag{3.6}$$

From Equation (3.4), time derivative of T is β. Together with Equation (3.2) and (3.5),

$$\frac{dr}{dt} = (\frac{E_a}{k_B}\frac{1}{T^2})\beta r + k_o e^{-\frac{Ea}{k_B T}} (-r) \tag{3.7}$$

With the property at peak,

$$\begin{aligned}
0 &= (\frac{E_a}{k_B}\frac{1}{T_P^2})\beta r + k_o e^{-\frac{Ea}{k_B T_p}} (-r) \\
(\frac{E_a}{k_o k_B}\frac{1}{T_P^2})\beta &= e^{-\frac{Ea}{k_B T_p}} \\
\ln(\frac{E_a}{k_o k_B}) + \ln(\frac{\beta}{T_P^2}) &= -\frac{Ea}{k_B T_p} \\
\ln(\frac{\beta}{T_P^2}) &= (-\frac{Ea}{k_B})\frac{1}{T_p} + \ln(\frac{k_o k_B}{E_a})
\end{aligned} \,.$$

By defining new variables as

$$Y = \ln(\frac{\beta}{T_P^2}) \quad , \quad X = \frac{1}{T_p} \tag{3.8}$$

we have a linear equation

$$Y = (-\frac{Ea}{k_B})X + \ln(\frac{k_o k_B}{E_a}) . \tag{3.9}$$

Thus, a measurement of the peak temperature at different heating rates can be used to determine the activation energy.

In my experiment, temperature is programmed with different heating rates β and an on-chip silicon diode is glued to the substrate for accurate temperature measurements. The desorption peak appears at different temperatures with different β. Fitting a set of β and T_p in Equation (3.9) yields the activation energy. Since the logarithm of the heating rate appears in Eq. 3.9, the heating rate needs to vary by at least two orders of magnitude for a reasonably precise measurement of E_a.

To maintain a constant heating rate (see Figure 3.6), the silicon heater requires constant heating power despite the constantly varying resistance of the silicon chip. I developed a GPIB program to monitor the voltage output and current in the heater in real-time mode (sampling at a typical time interval of 0.2 seconds). From the voltage and current, the resistance of the heater is calculated at each step and used to adjust the output voltage in the next step. The simple feedback mechanism can stabilize the heater at a constant power immediately after it is turned on.

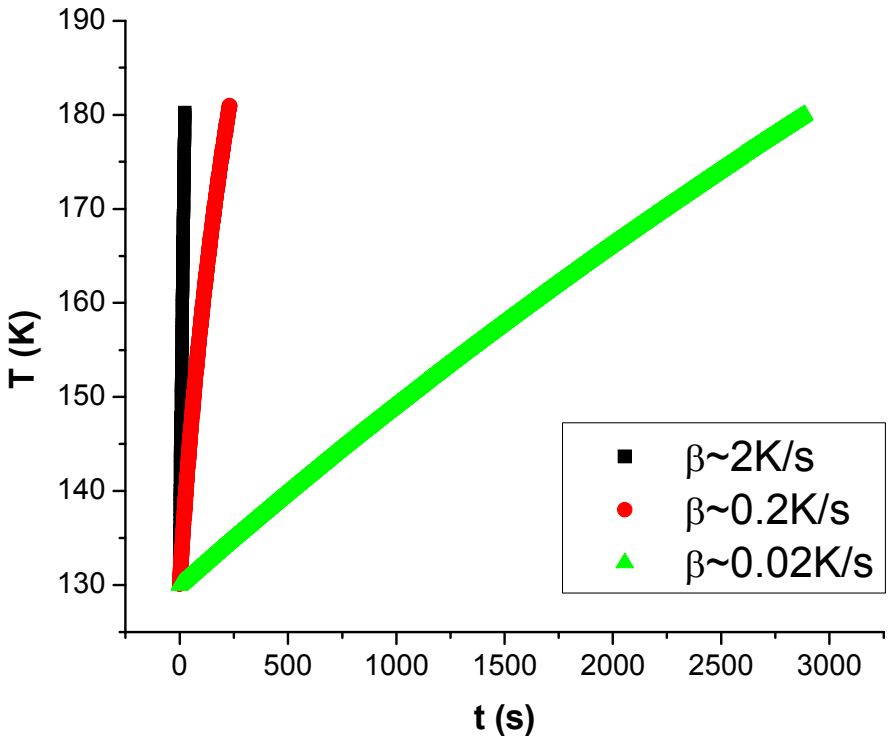

Figure 3.6 Controlled heating rates with a custom silicon heater.

Chapter 4 Charged impurity scattering in bilayer graphene

As discussed in Chapters 1 and 2, bilayer graphene (BLG)[30, 42] is a unique electronic material distinct from single-layer graphene (SLG)[9, 10]: while SLG has a massless, gapless electronic dispersion $E(k) = \pm\hbar v_F|k|$, BLG has a low-energy dispersion which is approximated[30, 43] by massive valence and conduction bands with zero gap: $E(k) = \pm\hbar^2k^2/2m^*$, where the effective mass is $m^* = \gamma_{inter}/2v_F^2$, with $\gamma_{inter} \approx 0.39$ eV the interlayer hopping matrix element, $v_F \approx 1.1 \times 10^6$ m/s the Fermi velocity in single layer graphene, and $\hbar$ Planck's constant. BLG has attracted interest because of a tunable bandgap[44-47], and unusual quantum Hall physics with an eight-fold degenerate zero energy Landau level[42, 48]. A recent review the electronic properties of bilayer graphene is available in Ref. [49].

However, when I began the work described in this chapter, little was known about disorder and charge-carrier scattering in BLG. Similar to SLG, BLG on SiO_2/Si substrates shows linear $\sigma(n)$[50], with mobilities limited to $<10^4$ cm^2/Vs. However, unlike SLG, linear $\sigma(n)$ is expected for both charged impurities and short-range scatterers within the complete screening approximation[31, 51, 52], hence the dominant disorder scattering mechanism in BLG cannot be determined from the linear $\sigma(n)$ alone. In this chapter I describe the first experiments to directly probe the effects of varying charged impurity density (through deposition of potassium) and dielectric constant (through deposition of ice) in BLG.

4.1 Potassium doping effect

4.1.1 Comparison with single-layer graphene

SLG provides a starting point for understanding the effects of disorder in BLG. As discussed in Chapter 2, in SLG on SiO_2 substrates[53] impurity scattering is dominated by charged impurities with a typical density n_{imp} of a few 10^{11} cm^{-2}, which gives rise to a linear conductivity as a function of charge carrier density, i.e. $\sigma(n) = ne\mu$ [54, 55] with constant mobility μ, with additional contributions from weak short-range scatterers with $\sigma(n) \sim$ constant[56]. At low n, the random potential from charged impurities produces electron and hole puddles with a characteristic carrier density n^*, giving rise to a minimum conductivity $\sigma_{min} = n^*e\mu \approx (4\text{-}10)e^2/h$. To leading order, $n^* \propto n_{imp}$ and $\mu \propto n_{imp}^{-1}$, so σ_{min} varies only weakly with n_{imp}[26, 54].

Charged impurities had been predicted to lead to stronger scattering in BLG compared to SLG[31], consistent with the generally lower mobilities observed for BLG compared to SLG. However, this prediction was based on two severe approximations for the bilayer case (complete screening, and zero impurity-graphene distance). Shaffique Adam, working with Michael Fuhrer and me, found that a more complete treatment indicates that BLG and SLG should have similar mobility for a similar density of charged impurity scatterers. The minimum conductivity of BLG with charged impurity disorder had also been studied theoretically. In contrast to SLG, the random charged impurity potential in BLG is well-screened, and $n^* = (n_{imp}/\xi^2)^{1/2}$, i.e. n^* is simply the fluctuation in the impurity number within an area given by the square of the puddle correlation length ξ. This leads to a strong prediction for the variation of the minimum conductivity on the density of trapped charges $\sigma_{min} \propto n_{imp}^{-1/2}$ which I test experimentally.

I experimentally measured the scattering rate for charged impurities on BLG by depositing potassium on BLG in ultra-high vacuum (UHV) at low temperature. Charged impurity scattering gives a carrier-density-dependent conductivity $\sigma(n)$ which is supralinear in n, with similar magnitude to single layer graphene for the measured range of carrier densities of 2-4 x 10^{12} cm^{-2}. The conductivity is in good agreement with that calculated within the Thomas-Fermi (TF) screening approximation[31] once the finite screening length and impurity-graphene distance are taken into account. The dependence of the minimum conductivity and the residual carrier density on charged impurity density are well-described by $\sigma_{min} \propto n_{imp}^{-1/2}$ and $n^* = (n_{imp}/\xi^2)^{1/2}$ in agreement with theoretical expectations, though the puddle correlation length ξ is significantly larger than predicted theoretically. The theoretical model ignores the opening of a band-gap, an approximation that is valid only when the disorder-induced potential fluctuation is much larger than the band-gap. The absence of any transport gap in our experiments suggests that the disorder potential is surprisingly large, and more work is needed to understand why the gapless model describes the experimental data. Most important, however, the experimentally measured magnitude and carrier-density dependence for charged impurity scattering on BLG indicate that unlike SLG, charged impurities alone cannot explain the observed transport behavior of *pristine* BLG samples on SiO_2, i.e. before the intentional addition of charged impurities. I infer the presence of an additional source of disorder in the undoped BLG that gives rise to $\sigma(n) \sim n$.

4.1.2 Potassium doping experiment

BLG is mechanically exfoliated from Kish graphite onto 300 nm SiO_2 on Si substrates. Figure 4.1a shows the BLG device used in this work, fabricated as described

in Chapter 3. Figure 4.1b shows the micro-Raman spectrum measured for this device. The Raman G' band can be fit with four Lorentzian components (Figure 4.1b); their relative peak positions and magnitudes are similar to those in Ref [35], and are indicative of Bernal stacking. After annealing in H_2/Ar at 400 ºC[37], the device was mounted on a cold finger in a UHV chamber and an overnight bakeout was performed in vacuum. In UHV, the charged-impurity density n_{imp} was varied systematically by deposition of potassium atoms from a controlled source at a sample temperature $T \sim 10$K. Conductivity as a function of gate voltage $\sigma(V_g)$ was measured *in situ* at different K concentrations; the carrier concentration is given by $n = (c_g/e)(V_g - V_{g,min}) = [7.2 \times 10^{10}\ cm^{-2}V^{-1}](V_g - V_{g,min})$ with $c_g = 1.15 \times 10^{-8}$ F/cm^2 the gate capacitance per unit area and $V_{g,min}$ the gate voltage of minimum conductivity.

Figure 2a shows $\sigma(V_g)$ measured at different K doses for BLG and, for comparison, Figure 2b shows similar data for SLG taken from Ref. [54]. Before K doping, the annealed BLG sample has a lower mobility (1,200 cm^2/Vs) than pristine SLG prepared similarly (13,000 cm^2/Vs). This is typical for H_2/Ar annealed BLG samples, which show mobility 2-5 times lower than un-annealed BLG, and ~10 times lower than SLG devices on the same SiO_2 substrates (annealing SLG does not appreciably change the mobility). K doping shifts the transport curve to the negative gate voltage side, lowers the mobility, decreases σ_{min}, broadens the minimum conductivity plateau and makes the $\sigma(V_g)$ curve nonlinear.

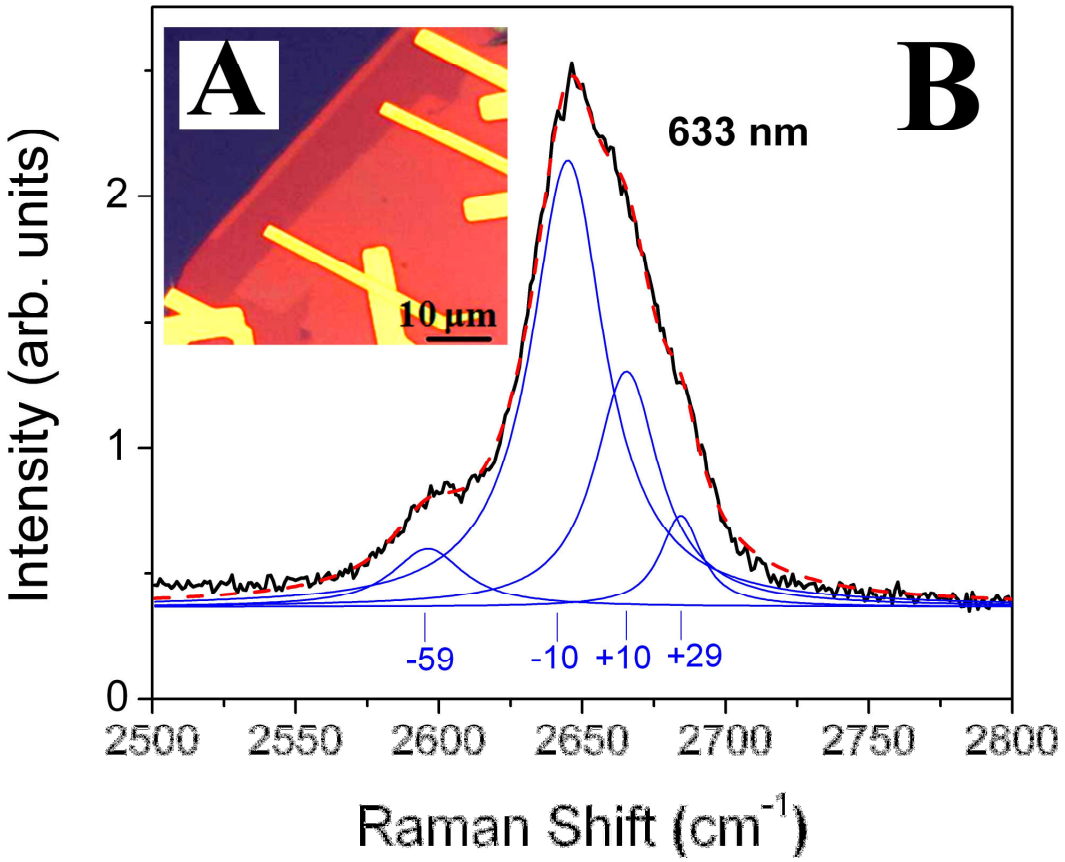

Figure 4.1 Bilayer graphene device.
(A) Optical image of the bilayer graphene (BLG) device. Dark blue area is thick graphite; red is the SiO_2/Si substrate, yellow areas are Cr/Au electrodes. The light purple rectangle is the bilayer graphene. (B) G' peak in micro-Raman spectrum acquired from the device area at 633 nm. Red line is fit to four Lorentzian components ; blue lines show the four individual components, numbers are relative offsets of each Lorentzian in cm^{-1}.

For uncorrelated impurities, the mobility is inversely proportional to the impurity density $\mu = \frac{C}{n_{imp}}$. The non-linearity of $\sigma(V_g)$ indicates that mobility, and thus C, is a function of carrier density, unlike SLG where C is a constant. To quantify my results I introduce an initial impurity density $n_{imp,0}$, so that the total impurity density is $n_{imp} = n_{imp,0} + n_K$, where n_K is the potassium concentration. While the charged impurities corresponding to $n_{imp,0}$ could in principle have opposite charge or be at a different distance from the bilayer graphene sheet than n_K, to avoid introducing too many

parameters, and consistent with results from residual impurities on single-layer graphene [56], I assume $\frac{1}{\mu(n)} = \frac{n_{imp,0}}{C(n)} + \frac{n_K}{C(n)}$. I assume that n_K is given by the shift of $V_{g,min}$, i.e. $n_K = (c_g/e)\Delta V_{g,min}$ which is exact within the parabolic approximation for the BLG Hamiltonian[31]; below it is shown that for the range of potassium densities I measure, this approximation remains very good for the hyperbolic Hamiltonian.

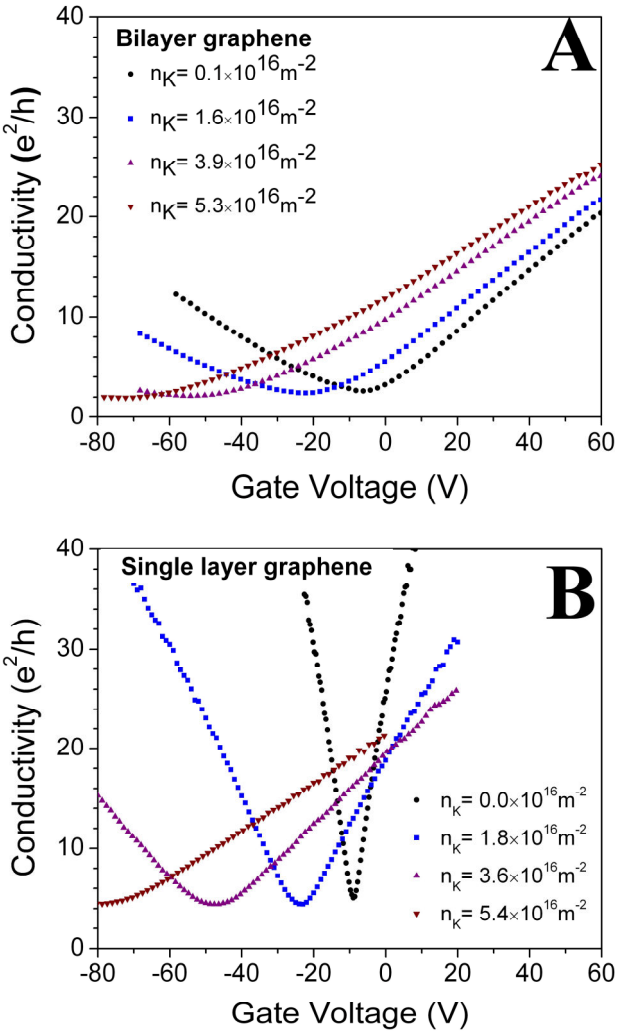

Figure 4.2 The conductivity (σ) versus gate voltage (V_g) curves for different potassium concentrations for BLG (A) and SLG (B). For BLG, $\sigma(V_g)$ is measured at a temperature of 10K in UHV. Data in (B) are from Ref.[54].

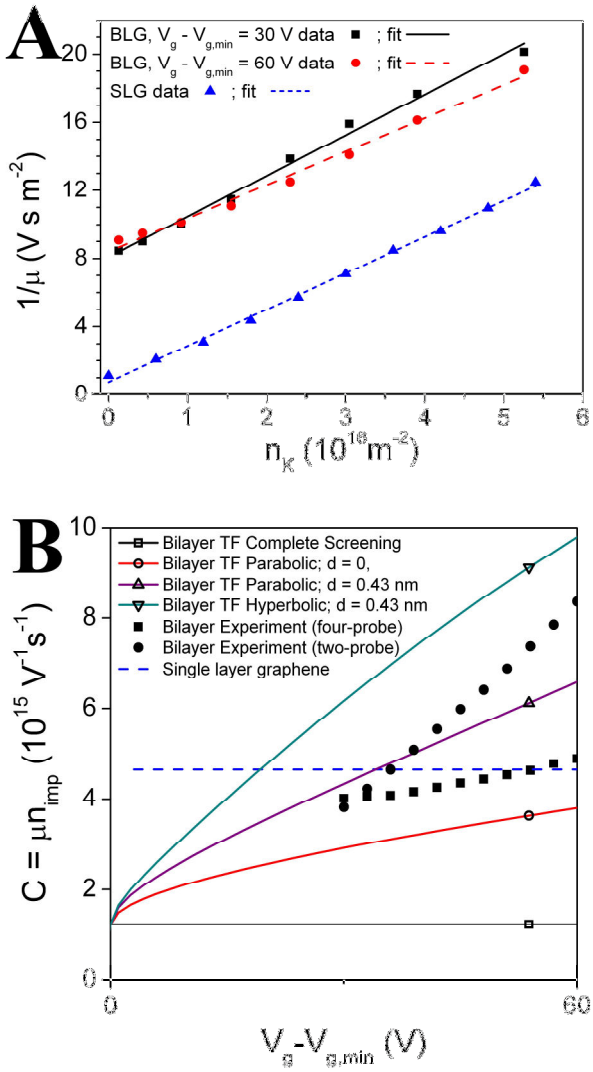

Figure 4.3 Analysis of scattering strength of BLG.
(A) Inverse of electron mobility $1/\mu$ versus potassium concentration n_K. Line are linear fits to all data points used to extract the slope $1/C$. μ is the maximum field-effect mobility for SLG (data from Ref. [54]) and is shown at two different carrier densities for BLG. (B) The inverse slope C from (A) versus effective gate voltage (solid black squares). Also shown is a second set of data from a different sample measured in a two-probe configuration (solid black circles). Solid lines show the theoretical predictions for C within the Thomas-Fermi approximation for a parabolic dispersion relation assuming complete screening (black line) and finite TF screening wavevector with impurity graphene distance $d = 0$ (red) and $d = 0.43$ nm (purple). The green line shows the theoretical results for a hyberbolic dispersion relation with finite TF screening wavevector and $d = 0.43$ nm. The SLG value is also shown (blue dashed line) for comparison[54].

Figure 3a shows the inverse electron mobility 1/μ as a function of n_K at $V_g = 30$ V and 60 V for BLG. 1/μ vs. n_K is linear as expected, and we determine $C(n)$ as the inverse of the slope of 1/μ vs. n_K, yielding $C(60\text{ V}) = 5.1 \times 10^{15}\ \text{V}^{-1}\text{s}^{-1}$ and $C(30\text{ V}) = 4.2 \times 10^{15}\ \text{V}^{-1}\text{s}^{-1}$. For $V_g < 30$ V the measurement is influenced by the minimum conductivity region, and 1/μ vs. n_K is not linear, so C could not be extracted. For BLG, $n_{imp,0}$ varies systematically from $3.4 \times 10^{16}\ \text{m}^{-2}$ at $V_g = 30$ V to $4.3 \times 10^{16}\ \text{m}^{-2}$ at $V_g = 60$ V. I find that the initial impurity density $n_{imp,0}$ for BLG is one order of magnitude higher than for SLG (see discussion below), the data for which are shown for comparison

Figure 3b shows the complete measured dependence of $C(V_g)$ for BLG (solid squares). Data from a second sample is also shown (solid circles), with similar results. For comparison, the SLG value, $C = 5 \times 10^{15}\ \text{V}^{-1}\text{s}^{-1}$ [54] is shown in blue. The similarity to the values for BLG indicates that the scattering cross section for charged impurities in BLG is very similar to SLG. The black line shows the previously calculated result[31] for $C(V_g)$ within the complete screening approximation with $d = 0$ (The calculation only considers the per-valley per-spin conductivity of BLG, which should be multiplied by four to obtain the total conductivity to compare with the measured values in this work.). The red and purple lines show $C(V_g)$ calculated by Adam within the Thomas-Fermi (TF) approximation without making the complete-screening approximation[31] for impurity-graphene distances $d = 0$ (red) and $d = 0.43$ nm (purple; the expected potassium-graphene distance of 0.26 nm[57] plus one-half the interlayer separation of 0.34 nm). The experimental data are close to the TF calculation with somewhat smaller magnitude and less carrier density dependence[58].

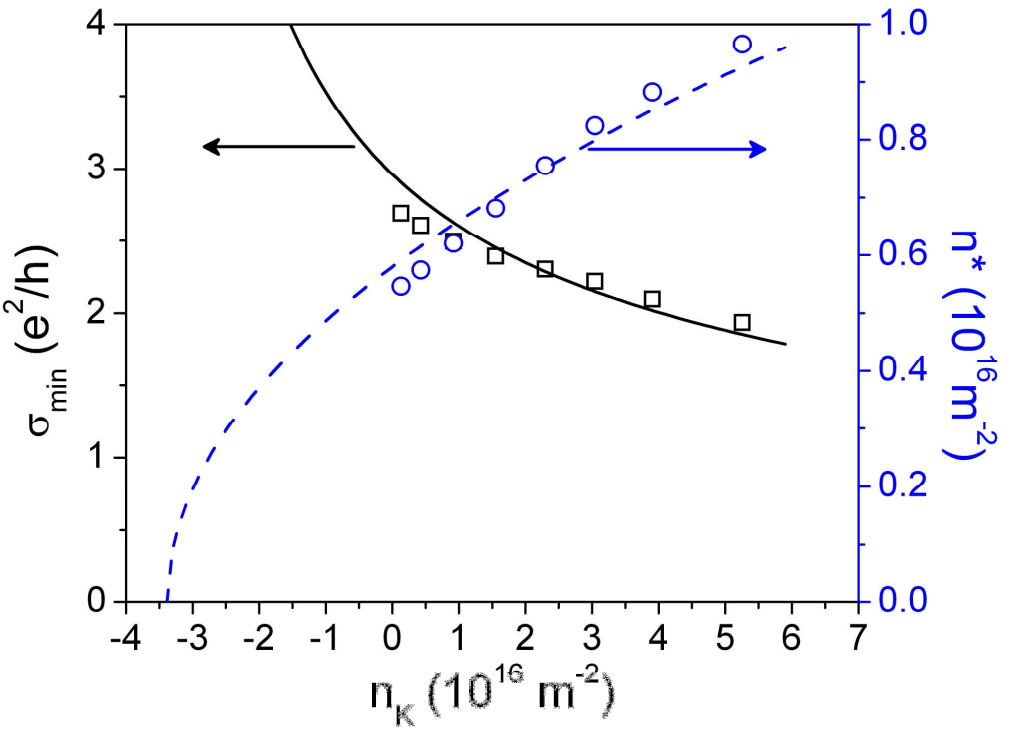

Figure 4.4 Minimum conductivity σ_{min} and residual carrier density n^* of bilayer graphene as a function of potassium concentration n_K. The blue (dashed) and black (solid) lines show fits to $n^* = [(n_{imp,0} + n_K)/\xi^2]^{1/2}$ and $\sigma_{min} = Ce[(n_{imp,0} + n_K)\xi^2]^{-1/2}$, with C and $n_{imp,0}$ determined from the fit to $1/\mu$ vs n_K at $V_g = 30$ V in Figure 3a, and $\xi = 32$ nm.

Figure 4 shows σ_{min} as a function of n_K. The minimum conductivity decreases with increasing charged impurity concentration. The residual carrier density is given by $n^* = \sigma_{min}/e\mu = \sigma_{min}(n_{imp,0} + n_K)/eC$. Since we do not know the mobility at $V_g = 0$, we use $C(30\text{ V}) = 4.2 \times 10^{15}\text{ V}^{-1}\text{s}^{-1}$ and $n_{imp,0}(30\text{ V}) = 3.4 \times 10^{16}\text{ m}^{-2}$ to estimate $\mu = C/(n_{imp,0} + n_K)$. Figure 4 shows n^* as a function of n_K. n^* increases with charged impurity doping, as expected. The solid lines in Figure 4 show fits to the theoretically predicted behavior $n^* = [(n_{imp,0} + n_K)/\xi^2]^{1/2}$ and $\sigma_{min} = Ce[(n_{imp,0} + n_K)\xi^2]^{-1/2}$. The only free parameter ξ is found to be 32 nm. This is significantly larger than the correlation length $\xi = 9$ nm calculated within the self-consistent model using TF screening. C is likely overestimated by as much as a factor of 3 in using $C(30\text{ V})$ (see Figure 3b), and therefore ξ may be as much

as 40% smaller (~18 nm), but still twice the calculated value. A similar discrepancy (self-consistent theory overestimating n^*) is found in SLG[54].

4.1.3 Discussion

The theoretical results discussed above rely on the parabolic approximation for the dispersion relation for BLG [30], only valid for carrier densities much lower than $n_0 = (v_F m^*/\hbar)^2/\pi \sim 2\times 10^{12}$ cm^{-2}. The experimental results presented here cross over from this low density limit to much higher densities where the parabolic approximation for the Hamiltonian breaks down. Adam has examined the robustness of the theoretical results for BLG transport at low density[31] to the situation when the carrier density (or equivalently, the impurity density) is much larger than n_0. His main finding is that the results for higher density are qualitatively very similar to those found using the parabolic approximation. The crossover Hamiltonian reads[30]

$H = \sigma_x \otimes [v_F(\sigma_x,\sigma_y)\cdot\hbar\vec{k}] + [(I_2 - \sigma_z)/2]\otimes\gamma_1\sigma_x$, where I_2 is the identity matrix and $\sigma_{x,y,z}$ are the Pauli matrices. The dispersion relation is hyperbolic, with $E_b = \hbar^2k^2/(2m^*)$ and $E_s = \hbar v_F|k|$ as the low density and high density asymptotes, where $v_F = 1.1\times10^6\, m/s$ is the SLG Fermi velocity and $m^* = \gamma_1/(2v_F^2) \approx 0.033 m_e$ is the low density effective mass for BLG. Analogous to the treatment in Ref[59] for SLG, for the crossover Hamiltonian the scattering time reads

$$\frac{\hbar}{\tau(\varepsilon(k))} = 2\pi\sum_{k'} n_{imp}\left|\frac{v(q,d)}{\varepsilon(q)}\right|^2 F(\theta)(1-\cos\theta)\delta(\varepsilon(k)-\varepsilon(k')), \qquad (4.1)$$

where the wavefunction overlap $F(\theta) = (1/4)[1-\eta+(1+\eta)\cos\theta]^2$, and $\eta = (1+n/n_0)^{-1/2}$ parameterizes the crossover. Within TF, the dielectric function

$\varepsilon(q,n) = 1 + v(q)\nu(n)$, and density of states $\nu(n) = (2m^*/\pi\hbar)\sqrt{1+n/n_0}$. The mobility calculated using Eq. 1 is shown in Fig. 3b (green line). As seen in the figure, while the modified Hamiltonian gives a slightly larger mobility, it is not significantly different from the low density parabolic dispersion approximation.

The transport properties at low density, close to the Dirac point, were also examined. Applying the self-consistent transport theory [26] to the parabolic approximation for bilayer graphene [31] gives $\bar{n} \equiv \left(\frac{c_g}{e}\right) V_{g,\min} = n_{imp}$ and $n^* = [n_{\rm imp}/\xi^2]^{1/2}$. Using the crossover Hamitonian the residual density is $n^* \approx n_{imp} C_0\left[\alpha\sqrt{n^*/n_0}\right] + \sqrt{4 n_{imp} n_0 C_0[\alpha\sqrt{n^*/n_0}]}$, where $\alpha = 4d\sqrt{2\pi n_0}$ and $C_0[x] = \partial_x\left[xe^x\int_x^\infty t^{-1}e^{-t}dt\right]$. The numerical solution for the electron and hole puddle density using the crossover Hamiltonian is remarkably close to the parabolic result $n^* = [n_{\rm imp}/\xi^2]^{1/2}$ with only about a five percent decrease in the value of ξ. The correction to $\bar{n}$ is more significant

$$\frac{\bar{n}}{n_{imp}} \approx \left[\frac{n_{imp}/n_0 + 4\sqrt{1+\sqrt{\beta n_{imp}}}}{4(1+\sqrt{\beta n_{imp}})}\right], \tag{4.2}$$

where $\beta = 1/\xi^2 n_0^2 \approx 6.4\times10^{-13}\,cm^2$, and the right hand side of Eq. 2 changes from unity at low impurity density to about 0.8 for the highest impurity densities we consider. This indicates that we may have underestimated the impurity concentration from $n_{\rm imp} = \bar{n}$ by up to ~20%, which would indicate that $C(n)$ may be higher than shown in Fig. 3b by up to ~20%.

4.1.4 Conclusion

Overall, the magnitude and carrier-density dependence of C and the impurity density dependence of n^* and σ_{min} are in good qualitative agreement with the theory of charged impurity scattering in BLG. However, C is somewhat smaller, and ξ somewhat larger, than expected theoretically, which both indicate that screening is not as effective as predicted. A possible explanation is the opening of a gap at the Dirac point in biased bilayer graphene[44-47], which we have not treated theoretically. The reduced screening in gapped BLG has also been put forth to explain the dependence of flicker noise on gate voltage in BLG[60]. One can expect that the signatures in transport experiments of the electric-field-induced band gap to be negligible when the disorder potential fluctuation is much larger than the band-gap (S. Das Sarma, private communication). From the optical measurements of Ref. [47] the maximum band-gap induced in the experiment can be estimated to be about 100 meV, while for $n_{imp} = 5.3 \times 10^{12}$ cm^{-2} , the unscreened disorder potential is estimated to be about 200 meV. Surprisingly, even though the band gap is similar in magnitude to the disorder potential, the theory which neglects the band gap describes the data reasonably well; more work is needed to understand this in detail. I expect the opening of a bandgap in BLG to have an even smaller effect on transport in the high-density regime (data in Figure 3b), where the change in density of states at the Fermi energy in BLG induced by gap opening is estimated to be a few percent.

Lastly, I discuss the nature of scattering in BLG on SiO_2. Our experimental finding that the magnitude of charged-impurity scattering in BLG is similar to SLG is surprising given that pristine BLG typically shows lower mobility (~10 times for our H_2/Ar annealed samples) than SLG on nominally identical SiO_2 substrates. I note that the

H_2/Ar annealing process itself significantly lowers the mobility of BLG (see Figure 4.5) without affecting SLG, which is not understood. The variation of C with V_g is also inconsistent with the linear $\sigma(V_g)$ observed in BLG[50]. Together, these observations indicate that another source of disorder may dominate BLG on SiO_2. This may be consistent with observations of reduced noise (presumably due to fluctuations of charged impurities) in BLG compared to SLG[61].

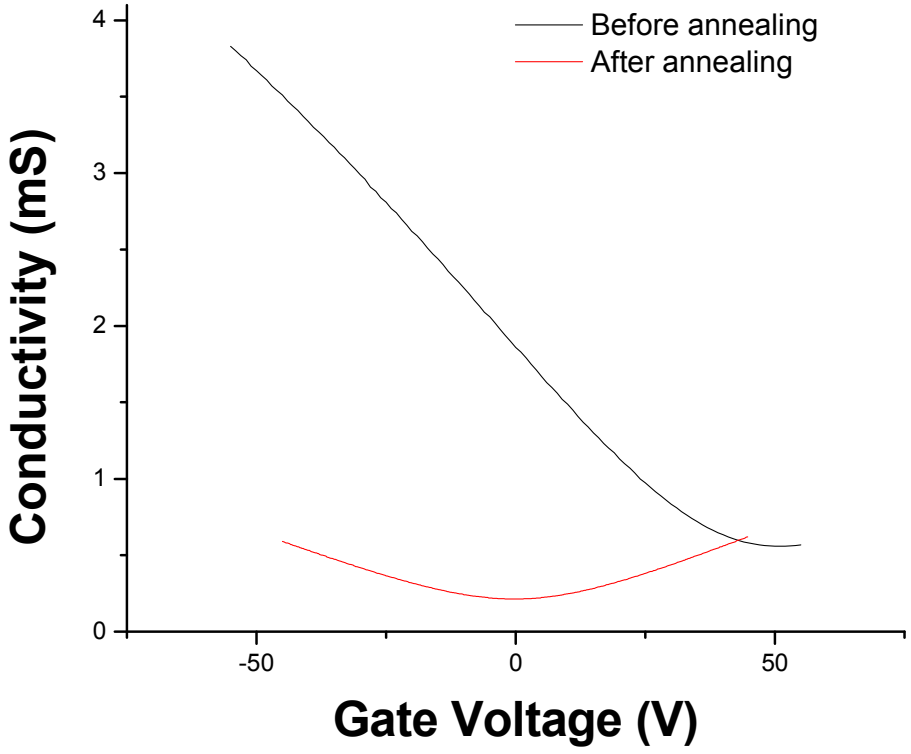

Figure 4.5 Annealing lowers the mobility of bilayer graphene devices.

4.2 Dielectric screening effect

Carriers in graphene are confined in an atomically thin plane. Changes in the dielectric background can tune the scattering strength in graphene.

Equation 2.2 in Chapter 2 is used for the conductivity with charged impurity (σ_l) in SLG, but it can be generalized to calculate the conductivity with short-range disorder (σ_s)[28]. For charged impurity, the dielectric background directly screens the Coulomb potential (see the function form of *V(q)* in Chapter 2) and changes the electron-electron Coulomb interactions which are represented in the electron screening *ε(q)* in graphene. For short-range impurity, the potential does not depend on the dielectric background, but the electrons are still interacting via Coulomb potential, hence the electron screening is affected.

In Ref. [56], the screening of SLG is investigated with adsorption of ice overlayers at low temperature. For both charged impurity and short-range impurity, the electron screening is weakened by additional screening from ice overlayers. Therefore σ_s is decreased, while σ_l is increased since the direct screening of the charged impurity overcomes the electron screening.

For BLG, with its massive dispersion relation, the electron-electron interaction barely changes with dielectric background, since the screening wavevector is roughly constant[62]. Direct screening of charged impurity should be the main effect.

Here I use ice deposited on bilayer graphene in UHV to modify its dielectric constant and observe the effects on its conductivity. The experimental setup is similar to that of the previous section. At low temperature, a leak valve introduces water vapor into the UHV chamber. The partial pressure of water is maintained at $\sim 1\times 10^{-8}\,Torr$ for short intervals to achieve sub-molecular layer control of the deposited ice.

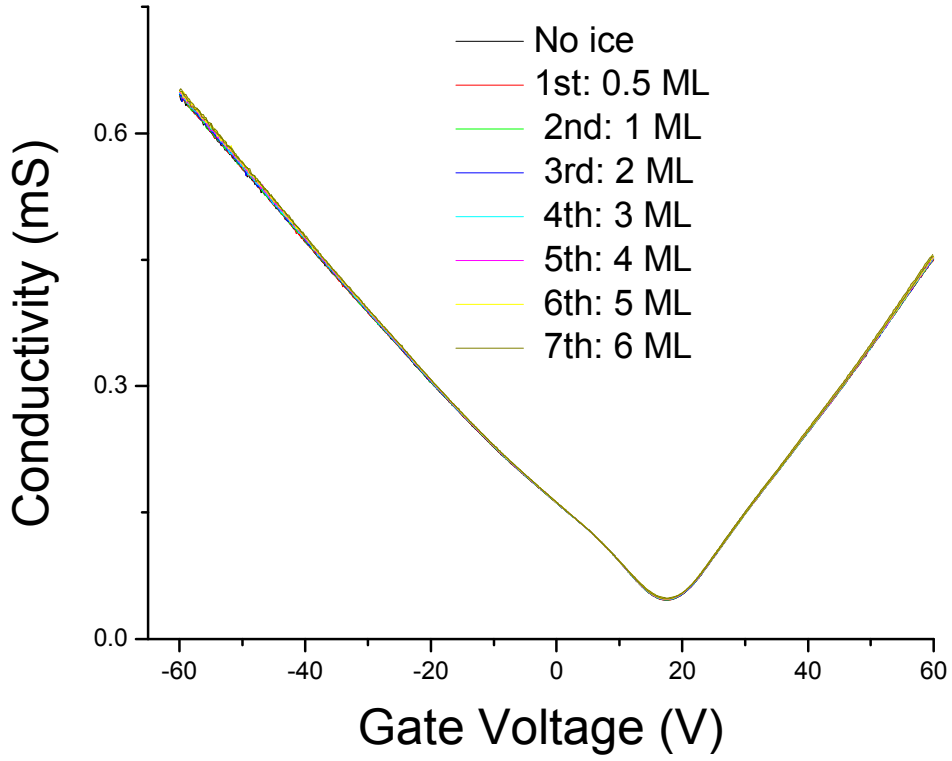

Figure 4.6 Ice deposition on bilayer graphene.

Figure 4.6 show the experimental conductance vs. gate voltage of bilayer graphene before and after ice deposition [one monolayer (ML) of ice corresponds to a density of $1\times10^{15}\,cm^{-2}$, the amount of ice deposited in 200 seconds at water partial pressure of $1\times10^{-8}\,Torr$]. The minimum conductivity appears at gate voltage $V_g = 18$V, which indicates the existence of a significant amount of charged impurities. However, after 6 layers of ice deposition, there is no measurable change in the conductance. The screening of charged impurities does not increase the device mobility. In Chapter 5 I show that ice deposited on BLG with adsorbed potassium *does* increase the mobility considerably, indicating that the screening of charged impurities by ice on BLG is

effective. Hence the data in Figure 4.6 indicate that charged impurities are not the dominant scatterers in pristine bilayer graphene.

Chapter 5 Dielectric screening of adsorbed potassium ions on graphene

As discussed in the previous chapter, dielectric screening effect has been observed in single layer graphene (SLG) by adding ice overlayers in ultrahigh vacuum (UHV) at low temperature[56]. In Ref.[56], the field effect mobility is limited by long-range scattering from charged impurities in SiO_2 substrate underneath graphene. Adsorbed water increases the background dielectric constant, reduces the Coulomb interaction between electrons and charged impurities and enhances the mobility by over 30%.

In the previous chapter, I showed that the addition of ice overlayers to pristine BLG in UHV has little effect on the conductivity suggesting that charged impurities have a minor role in the disorder of pristine BLG on SiO_2/Si. In this chapter I discuss the adsorption of ice on SLG and BLG with known quantities of potassium already deposited in UHV as in Chapter 4. In potassium adsorption experiments [54, 63], on both SLG and BLG each adsorbed potassium atom transfers ~1 electron (at low coverage) to graphene and the resulting potassium ion acts as a charged impurity above graphene [57]. I find that the adsorbed ice adlayers screen the Coulomb potential of the adsorbed potassium ions very efficiently, leading to mobility increases larger than predicted using the bulk dielectric constant of ice ($\kappa = 3.2$). This suggests that the dipolar water molecules rearrange in proximity to the impurities, and provide additional screening.

The screening effect of ice is observed on both K-doped SLG and BLG. The fact that the screening effect of ice is significant for pristine SLG, but absent for pristine BLG, suggests that another disorder mechanism is dominant in pristine BLG.

5.1 Coadsorption of water with potassium

Coadsorption of water with alkali metal atoms on metal and nonmetal substrates has been widely studied [64] with surface science techniques. Two types of interactions of alkalis with water are closely related to the experiments in this chapter.

First, alkali-induced dissociation of water changes the interaction between the substrate and adsorbed water and may form alkali hydroxides[65]. This process is found to require a critical coverage of preadsorbed alkali at low temperature. For potassium, $\theta_{K,crit} \sim 0.1ML$. A widely held explanation is that the dissociation of water is induced by the electric field between alkalis on a substrate[64].

Second, water is highly efficient at screening the bare Coulomb potential of the alkali metal through rearrangement of dipoles or ions. This effect is termed "hydration", which is defined, originally for solutions, as the process of attraction and association of water molecules with molecules or ions of a solute. In coadsorption systems, water molecules interact with the ions in a similar way as in solution and form hydration shells[65, 66] around the ions.

5.2 Screening of adsorbed potassium ions on SLG

I first discuss the coadsorption of potassium and ice on SLG. Graphene is pre-covered with a very low dose of potassium ($\theta_K \sim 0.001ML$) at low temperature (~20K) in UHV in the same fashion as described in Ref. [54] and in the previous chapter. Water vapor is introduced into the UHV chamber via a leak valve, which can control the water partial pressure from $1\times10^{-9}Torr$ to $1\times10^{-7}Torr$. Water overlayers are frozen on the cold graphene sample as well as the whole cold finger (see Figure 5.1). The thickness of

adsorbed water is estimated by the partial pressure of water and the "on" time of the leak valve, under assumption of a uniform and layer-by-layer adsorption.

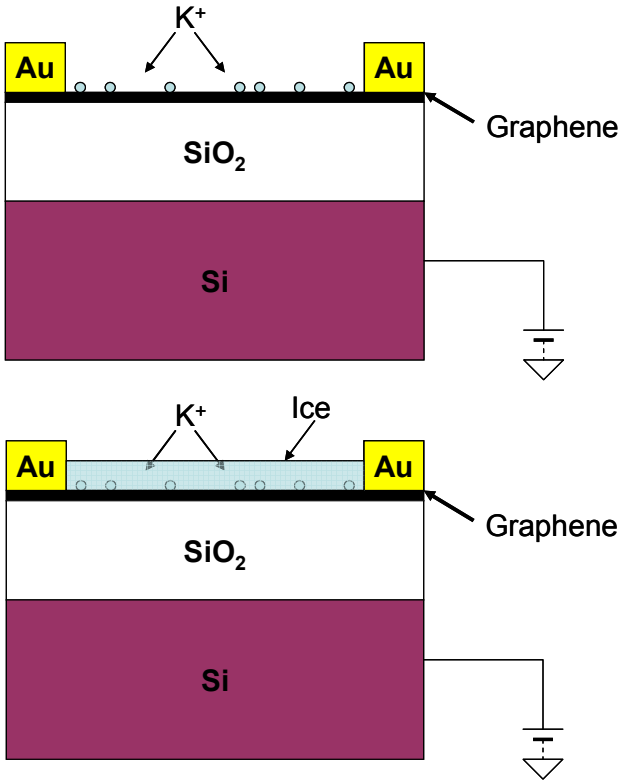

Figure 5.1 Schematics of potassium adsorption (top) and coadsorption of water with potassium(bottom).

Figure 5.2 shows the experimental data of water deposition on potassium-doped graphene. At low temperature, potassium adatoms dope the graphene device, shift the Dirac point to the negative side and reduce the field effect mobility by about one order of magnitude, as observed in Ref. [54] (Figure 5.2 upper panel). After additional deposition of water, the doping as measured by the Dirac point shift doesn't change (see Figure 5.2 lower panel), which indicates there is no chemical reaction of water with potassium. In these experiments the potassium concentrations are less than 4.2 x 10^{12} cm^{-2}, or less than 0.009 ML. Thus, the finding that water does not react with potassium is consistent with

the previous observations of a critical coverage of ~0.1 ML required for water dissociation[65].

Multiple depositions of ice have been performed until the $\sigma(n)$ curve saturates. At this coverage the mobility is observed to have increased by about 400% compared to the value before ice deposition (but after potassium deposition). This compares to the mobility increase of 30% found in Ref. [56] for ice screening on pristine graphene (presumably screening charged impurities in the SiO_2). I hypothesize that the difference arises due to the direct contact between water molecules and bare potassium ions. When a water molecule adsorbs near a potassium ion, with the help of the initial kinetic energy at landing it can rearrange the orientation of its dipole to align with the local electric field. In this way, the adsorbed water screens the dominant charged impurities (the potassium ions) much better than in the case of background dielectric screening. After coadsorption, the $\sigma(n)$ curve is not linear at low carrier density, which indicates carriers with higher Fermi wavevectors experience a weaker Coulomb potential and there exists a length scale for the hydration regions around the potassium ions. In Ref. [56], the graphene device has been cleaned to expose the carbon atoms and the dominant scatterers are the charged impurities under the graphene sample. Theoretical estimates of the graphene-impurity distance are on order 1 nm[26], significantly farther from the water molecules than the potassium ions which sit on top of graphene. Therefore, there is no strong local electric field to make water molecules reorient.

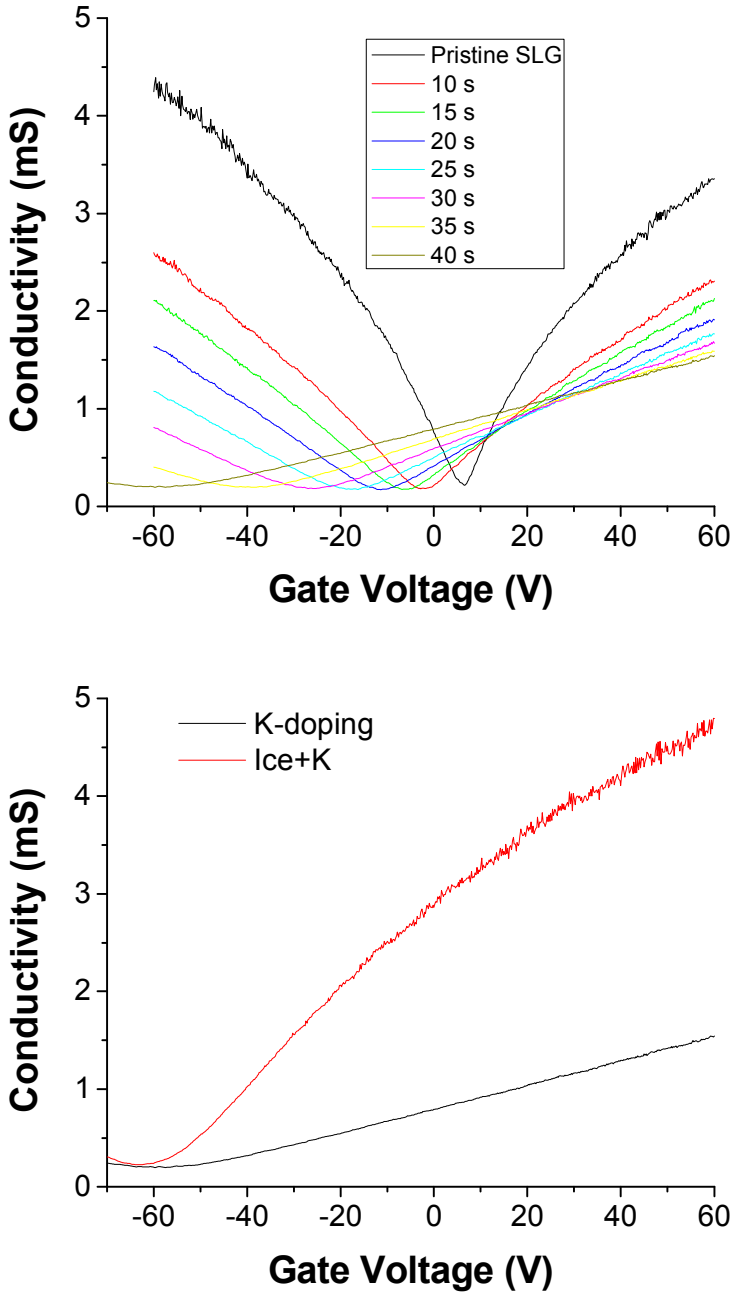

Figure 5.2 Effect of potassium adsorption (top) and water coadsorption with potassium (bottom) on SLG. In top panel, different colors correspond to different adsorption times (amounts of adsorbed potassium) as shown in the legend. Data are taken at a temperature of 20 K. In bottom panel, the black curve shows SLG after potassium adsorption only, and the red curve after potassium adsorption plus the addition of 12 monolayers of ice. Data are taken at a temperature of 20 K.

In Ref. [67], hydration of potassium has been reported as the delayed water desorption peak in temperature programmed desorption (TPD) data, after coadsorption of water with potassium at 110K. The hydration may also exist in our experiment. However, at 20K water molecules are frozen and cannot fully hydrate the potassium ions. The initial dipole reorientation upon adsorption is still the dominant effect.

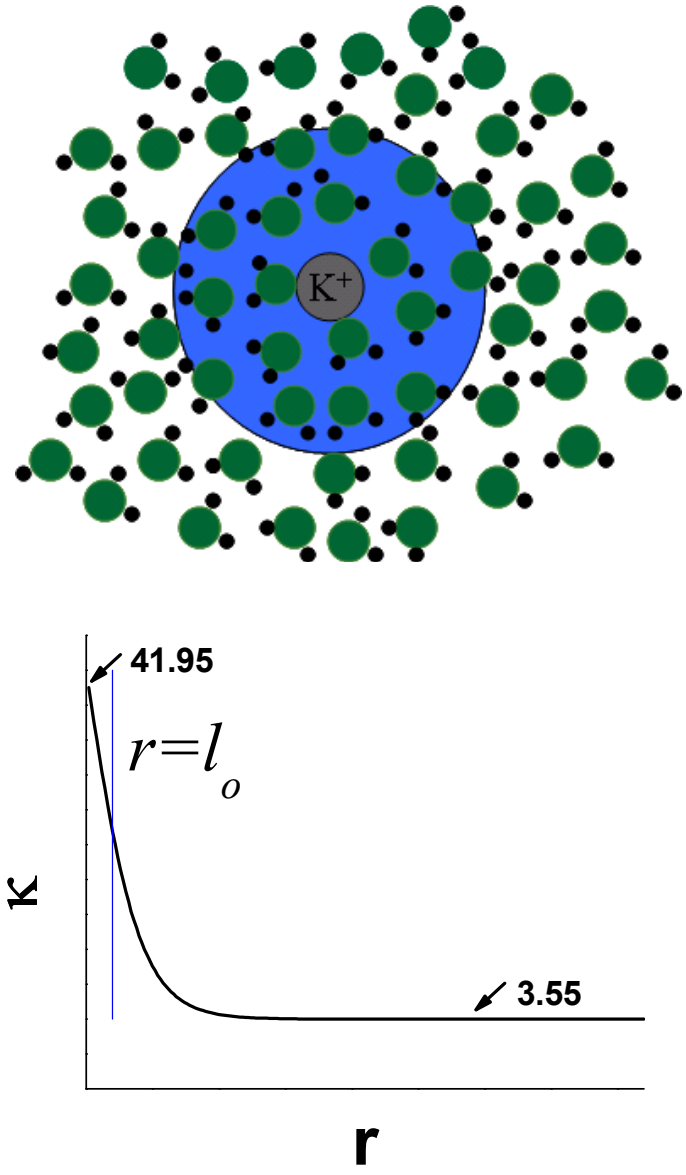

Figure 5.3 Hydration effects in the coadsorption complex of potassium and ice. In the schematic (top), the blue region represents the hydration shell around a potassium ion. Corresponding dielectric constant (bottom) is modeled with a sigmoid form function.

I have modified the theoretical model of SLG (see Chapter 2) with a phenomenological Coulomb potential to explain the experimental data. In the way the coadsorption complex forms, water molecules near potassium ions can align their dipoles to local electric field from potassium ions, just like in solution. Therefore, the dielectric constant is increased in the hydration region (see Figure 5.3). The water near potassium ions is still amorphous ice as in the bulk of ice overlayers, but the dipoles of the water molecules are ordered to screen the potassium. I assume the ice dielectric constant is close to that of liquid water ($\kappa_{hyd} = \kappa_{water} = 80$) near the potassium ions and normal ($\kappa_{ice} = 3.2$) in ice far away. To avoid any sharp change in Coulomb potential, I adopt a sigmoid form function for the effective dielectric constant

$$\kappa(r) = \frac{2\left(\left(\frac{\kappa_{hyd} + \kappa_{SiO_2}}{2}\right) - \left(\frac{\kappa_{ice} + \kappa_{SiO_2}}{2}\right)\right)}{1 + e^{r/l_o}} + \frac{\kappa_{ice} + \kappa_{SiO_2}}{2}, \tag{5.1}$$

where κ_{SiO_2} is the dielectric constant of SiO_2 and l_o is the radius of the region with high dielectric constant. At r<< l_o, $\kappa(0) = \frac{\kappa_{hyd} + \kappa_{SiO_2}}{2}$ and at r>> l_o, $\kappa(\infty) = \frac{\kappa_{ice} + \kappa_{SiO_2}}{2}$, which are the effective dielectric constants at the hydration shell and SiO_2 interface and the normal ice and SiO_2 interface[56], respectively.

Now the 2D Fourier transform of Coulomb potential does not have a simple analytical form as in Chapter 2. I define

$$G(q) = \kappa(\infty)\int_0^\infty \frac{J_o(x)}{\kappa(\frac{x}{q})}dx\,. \tag{5.2}$$

The new form of the Coulomb potential modifies Equation (2.2) in Chapter 2 by replacing q with $q/G(q)$. Hence I can calculate the conductivity from long-range scattering $\sigma_l(n_{imp}, l_o)$.

Numerical calculation has been performed with the form[56] (see discussion in Chapter 2)

$$\sigma^{-1} = \sigma_l^{-1}(n_{imp}, l_o) + \sigma_s^{-1}, \tag{5.3}$$

where n_{imp} is estimated from $V_{g,,min}$. At low carrier density, the mobility strongly depends on l_o and $l_o = 3a$ generates the best fit. With reasonable short-range scattering

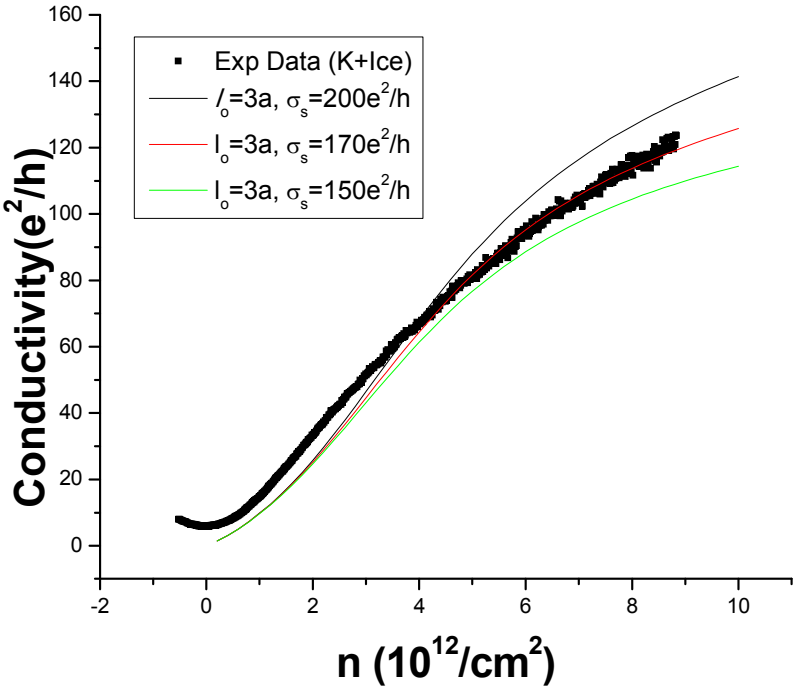

Figure 5.4 Conductivity vs. carrier density for graphene with coadsorbed potassium and ice. Experimental data are black squares. Lines are numerical calculation of the mobility with the phenomenological Coulomb potential derived from Eq. 5.1. The charged impurity density 4 x 10^{12} cm^{-2} is estimated from $V_{g,min}$. The length scale $l_o = 3a$, with a = 0.246 nm the graphene lattice constant, is chosen to fit the mobility at low carrier density. The three lines are fits using different values of the conductivity limited by short-range scatterers.

conductivity, the model can explain the experimental data very well (see Figure 5.4). The length scale l_o is consistent with the radius of the second hydration shell in *ab initio* simulations[66].

While the model is quantitative, it indicates an increase of the dielectric constant of ice at very short length scales (corresponding to a few graphene lattice constants or a few water molecules) can account for the large increase in mobility. The fact that l_0 is less than 1 nm indicates that the hydration effect is large for potassium adsorbed directly on graphene, but could be small for charged impurities under the graphene in the SiO_2, consistent with previous observations of screening of pristine graphene on SiO_2 with ice[56].

5.3 Screening of adsorbed potassium ions on BLG

As shown in Chapter 4, the mobility due to scattering by the same concentration of charged impurities is similar for BLG and SLG. Yet BLG is observed to have significantly lower mobility on SiO_2, and ice adsorption has no effect on the mobility of pristine BLG. Together the observations indicate that for pristine BLG, charged impurities are not the dominant scatterers. After potassium doping[63], the mobility of BLG lowers by a factor of 2, hence charged impurities start to play an important role in determining the transport properties. I studied co-adsorption of potassium and ice on BLG under conditions similar to those described above for SLG.

Figure 5.5 shows the results of potassium adsorption on BLG (top panel) followed by ice adsorption on K/BLG (bottom panel). In contrast to ice adsorption on pristine BLG (Chapter 4), ice strongly increases the mobility in K/BLG. In fact, the same hydration effect as observed in SLG makes the ice deposition screen the potassium ions so well that

the device mobility is essentially restored to the value of pristine BLG (see Figure 5.5, inset to bottom panel).

The screening effect of ice on K/BLG experimentally proves that charged impurities on BLG can indeed be screened by a dielectric background. Together with the ice deposition experiment on pristine BLG (Chapter 4), it further confirms that charged impurities are not the dominant scatterers in pristine BLG.

The hydration effect can be qualitatively explained with the same dielectric model as in SLG; one expects again a large increase in mobility for the charged-impurity portion of the scattering once ice is added. This is consistent with the observed return of the conductivity to a level close to that of pristine graphene (without added K or ice; see Figure 5.5 bottom inset). However, it is difficult to make a quantitative comparison to my model, since the dominant scattering mechanism in BLG is still not clear. Additionally, it is evident that other effects need to be considered. At low carrier density, the ice deposition lowers the minimum conductivity by a factor of 3, which makes the apparent field effect mobility even higher than seen in pristine BLG. The change in minimum conductivity could be due to the opening of a gap at the Dirac point in BLG[45] due to the perpendicular electric field generated by the potassium ions and gate. This can seriously affect the l_o in fitting.

Recent experiments have achieved high-quality BLG devices on hexagonal boron nitride (h-BN) substrates[68] with mobility ~ 100,000$cm^2V^{-1}s^{-1}$, comparable to or even greater than that found for SLG on h-BN. This might point to corrugations in the BLG resulting from adhesion to rough SiO_2 as the dominant scatterers in BLG on SiO_2, since SiO_2 is much rougher than h-BN substrate which is nearly atomically flat.

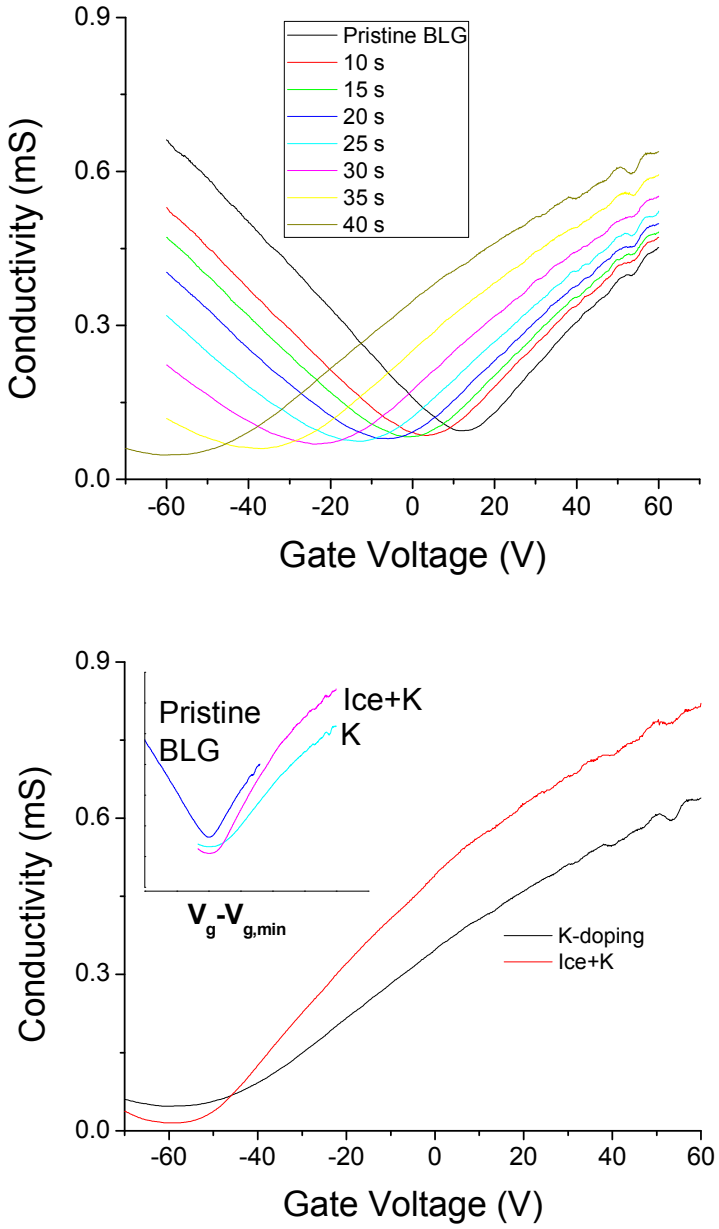

Figure 5.5 Effect of potassium adsorption (top) and water coadsorption with potassium (bottom) on BLG. In top panel, different colors correspond to different adsorption times (amounts of adsorbed potassium) as shown in the legend. Data are taken at a temperature of 20 K. In bottom panel, the black curve shows BLG after potassium adsorption only, and the red curve after potassium adsorption plus the addition of 10 monolayers of ice. Data are taken at a temperature of 20 K. The inset in bottom panel shows the shifted transport curves (conductivity versus gate voltage measured from the minimum conductivity point) of pristine BLG, K/BLG and Ice+K/BLG for comparison.

Chapter 6 Temperature-dependent phenomena in coadsorbed ice and potassium on graphene: solvation, desorption and reaction

The graphite surface has been employed to study surface science as an ideal platform that is both chemically stable and perfectly flat[57]. Graphene not only inherits this merit from graphite, but provides an all-surface material whose electronic properties are extremely sensitive to the changes on its surface. This is demonstrated dramatically already in Chapters 4 and 5, where graphene's electronic properties respond significantly to ~1 ML of dielectric material, and to as little as 0.001 ML of charge-transferring adsorbates[54, 56]. This chapter steps forward to discuss the effects of solvation, desorption and reaction on the electronic properties of graphene and demonstrate that electronic signals from a graphene device can be used to detect various surface science phenomena.

In this chapter, experiments with different adsorbates are discussed separately since their interactions with graphene vary dramatically. Section 6.1 probes the behavior of coadsorbed ice and potassium at desorption and compares with desorption of adsorbed potassium without ice overlayers. Section 6.2 describes phase transitions of ice and the influence of oxygen impurities. Section 6.3 covers the adsorption and desorption of molecular oxygen.

6.1 Desorption of coadsorbed ice and potassium

Chakarov and coworkers[65, 69] studied the coadsorption of H_2O and K on C(0001) (graphite) at low temperature and potassium coverages from 0.2 to 0.6 ML. They noticed two behaviors upon warmup: phase transition of ice and hydration of

potassium. At low K coverage (<0.3ML) with no ice present, K atoms are nearly ionized and well separated from each other. After additional ice adsorption, water molecules adsorbed near a K adatom orient their dipoles to screen the Coulomb potential of the K ion (as discussed in the previous chapter in this thesis) and partially hydrate the K ion. Chakarov et al. found no dissociation of ice from their high resolution electron energy loss spectroscopy (HREELS) at low K coverage, which is consistent with other experiments on metal substrates[64]. In their water desorption experiment[69], water deposited (without potassium) at 85 K was found to form 2D amorphous ice and upon warmup to undergo an amorphous-to-crystalline ice phase transition around 135 K (at a heating rate ~2 K/s), followed by desorption of water at 150 K. The crystalline phase dewets the surface and forms three-dimensional (3D) islands. In contrast, in desorption of ice and potassium complexes[65], the water molecules near K ions are stabilized by the hydration and desorb at a higher temperature of 180 K. The experiments of Ref. [65] also show a desorption peak of K ions at 135 K in temperature-programmed desorption that is explained by exothermic rearrangement of ice-potassium complexes.

I have studied the temperature and carrier-density dependence of the conductivity of graphene with coadsorbed potassium and ice. Figure 6.1 shows representative temperature-dependent transport curves of graphene with the coadsorbate system. In Figure 6.1, coadsorption of ice (18 ML) with dilute K (0.01 ML) has been prepared in UHV and at low temperature (see previous chapter for details). The conductivity at different gate voltages is measured while the system is warming up. Because the temperature is changing during data collection, the temperature for each curve is accurate to within ~5 K. In agreement with the results of the previous chapter, the doping due to

potassium persists after ice deposition (the gate voltage of minimum conductivity $V_{g,min}$ does not shift). As the temperature is raised, the doping persists ($V_{g,min}$ stays the same) but the conductivity outside the minimum conductivity plateau increases with rising temperature up to 143 K. At 143 K, $V_{g,min}$ suddenly moves ~40V toward zero gate voltage, which indicates the removal of 2/3 of the doping caused by the potassium adatoms. We identify the sudden shift in doping at 143 K with the amorphous-to-crystalline phase transition of the ice overlayers.

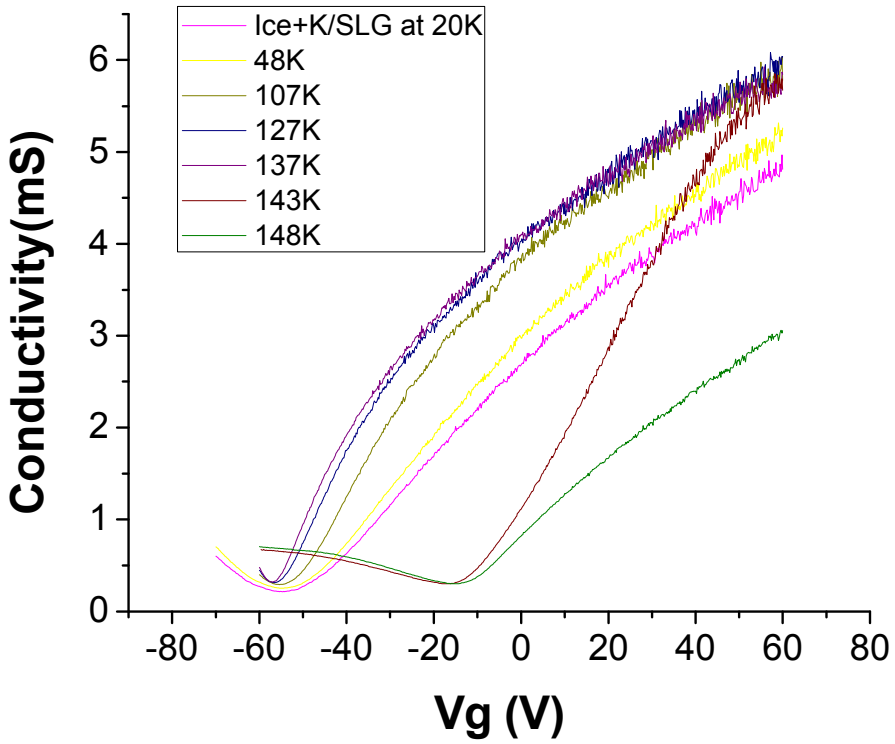

Figure 6.1 Impact of coadsorbed ice and dilute potassium on electronic properties of graphene at different temperatures. The coadsorbed potassium and ice on SLG was prepared at 20 K in the same manner as described in Chapter 5. The potassium concentration is estimated from the $V_{g,min}$ shift to be ~4 x 10^{12}/cm^2, which corresponds to a coverage of 0.01 ML. The ice coverage is 18 ML.

Imprisoned by ice, the K ions can not easily move on the graphene surface. They remain in the same random distribution as long as they are covered by solid ice. The observed increase of conductivity is therefore not likely due to the correlation of K ions[29]. Instead it could be explained by hydration of K ions and the rearrangement of hydrated K ions. At adsorption temperature (20K), the ice molecules adsorbed near K ions might not be able to fully align their dipoles to the Coulomb potential of K ions. At higher temperatures the partially hydrated K ions are thermally annealed forming a full hydration shell around K ions, which further screens the electric field of K ions. The fact that structural phase transition to crystalline ice and rearrangement of hydrated K ions both happen near 135 K in Ref [65, 69] indicates that some hydrated K ions might be rearranged and hence move into the bulk of the ice during the transition from 2D amorphous ice to 3D crystalline ice, which would increase the distance between K ions and graphene. Better screening of charged impurities and increased distance between graphene and charged impurities both reduce the scattering of carriers by K ions and increase the conductivity.

In Figure 6.1 the doping level remains the same below 140 K, indicating little desorption of K, probably because the K ions are buried under thick ice overlayers. Upon the amorphous-to-crystalline transition, which is accompanied by dewetting, there is significant rearrangement of the ice and, I presume, the K atoms. After losing direct contact with graphene, K ions could desorb as observed in Ref. [65]. From the change of conductivity, I find that most of the K ions (~2/3) are desorbed at the phase transition of ice. This is not consistent with the result in Ref. [65], where only a small amount of K

ions desorbs. However, the difference may arise from the fact that the potassium coverage in this experiment is 2 order of magnitude lower than in Ref. [65].

The system is heated up at a rate of ~0.02K/s. At this heating rate, it is reasonable to expect that ice desorbs from graphene at about 140K[69-71], though there is no direct evidence of desorption in this experiment. The desorption of ice could therefore be an alternative explanation for the sudden change of doping level around 143K . However, further experiments on desorption of ice alone (see Section 6.2 below) suggest that the desorption of potassium may be related to the phase transition of ice. The phase transition and desorption could be a continuous process and they can overlap each other for thick ice. During the process, some K ions in the ice crystal either react with ice or desorb together with water molecules and some hydrated K ions are left on graphene as observed in Ref. [65].

To further explore the dramatic change around 143K, I performed temperature programmed desorption (TPD). Since I introduce water vapor into the whole chamber, at low temperature all the cold surfaces are covered with ice. As the system is heated up, the mass spectrometer measures the water desorption from the whole cold finger. In the measured partial pressure, contribution from ice deposited on the micron-size graphene surface is negligible, and therefore the desorption peak measured by the mass spectrometer does not necessarily coincide with the desorption of ice from graphene. Instead I use the electronic properties of graphene to monitor the desorption. I monitor the resistance at zero gate voltage as a function of temperature. Figure 6.2 shows such a measurement of the resistance of graphene at fixed gate voltage (V_g=0) as a function of temperature for coadsorbed K (~0.01 ML) and ice (10 ML). At low temperature, the

minimum conductivity point is far from zero gate voltage (the sample is highly doped by potassium) and the resistance is low mainly because of this high carrier density. At the desorption temperature, the minimum conductivity point moves close to zero gate voltage and the resistance increases.

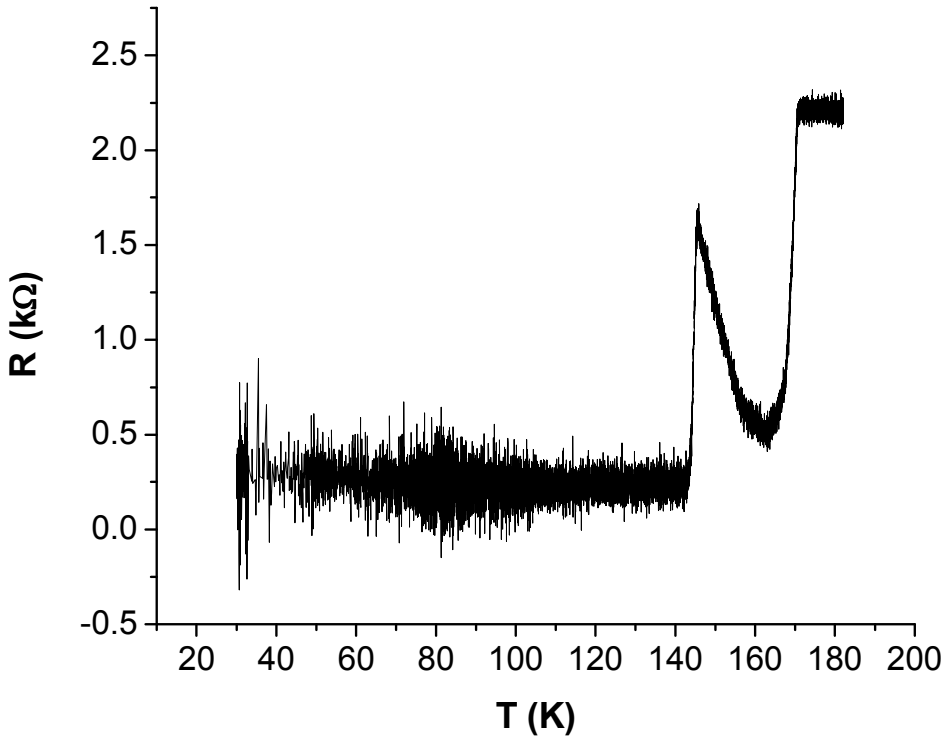

Figure 6.2 Electronic monitoring of the desorption of coadsorbed ice and potassium. ~0.01 ML of K and 10 ML of ice are deposited on graphene at 30 K. The resistance of graphene at zero gate voltage is measured as a function of temperature. Temperature is increased at a rate of ~0.02 K/s.

After the increase of resistance at about 145 K due to Dirac point shifting toward zero gate voltage, there is a slow decrease in resistance and then another increase. These features can be just fluctuations of adsorbates after ice desorption (see discussion in Section 6.2), although the second increase near 170K may be related to the desorption of ice from hydrated K ions observed in Ref. [65].

Figure 6.3 shows thermally activated behavior of desorption using TPD (see discussion in Chapter 3). Only the first increase of resistance has reasonable shift in temperature at different heating rates. The slope maximum in Figure 6.3 (top) is used to identify the position of this feature as an effective "peak" position in conventional TPD. (see Table 6.1)

The "peak" temperature T_p and heating rate β are converted to $X = \ln(\beta/T_p^2)$ and $Y = 1/T_p$ in Table 6.1 as formulated in Chapter 3. Figure 6.3 (bottom) shows the linear fitting to extract the slope as $-E_a/k_B$ = -6400 K and E_a = 0.55eV. The activation energy is comparable to the desorption energy of 0.45eV per ice molecule in Ref. [69] and suggests that the rate limiting process here is the breaking of hydrogen bonding in ice.

Peak Temperature T_p (K)	Heating Rate β (K/s)	$Y= \ln(\beta/T_p^2)$	$X= 1/T_p$
164.4	1.75363	0.00608	-9.64292
154.7	0.25218	0.00646	-11.4606
148.2	0.01847	0.00675	-13.9887

Table 6.1 Fitting variables X and Y for coadsorption experiments.

Figure 6.4 shows similar desorption measurement of potassium adatoms without ice overlayers. From experimental data there is continuous change of doping from 140 K to room temperature. In Ref. [65], potassium desorbs from graphite at higher temperature with desorption peak at 420 K. The difference suggests that the observed doping change is not the effect of desorption. Rather, I suppose that potassium adatoms could start to move on graphene at rising temperature and run off the micron-sized device before desorption.

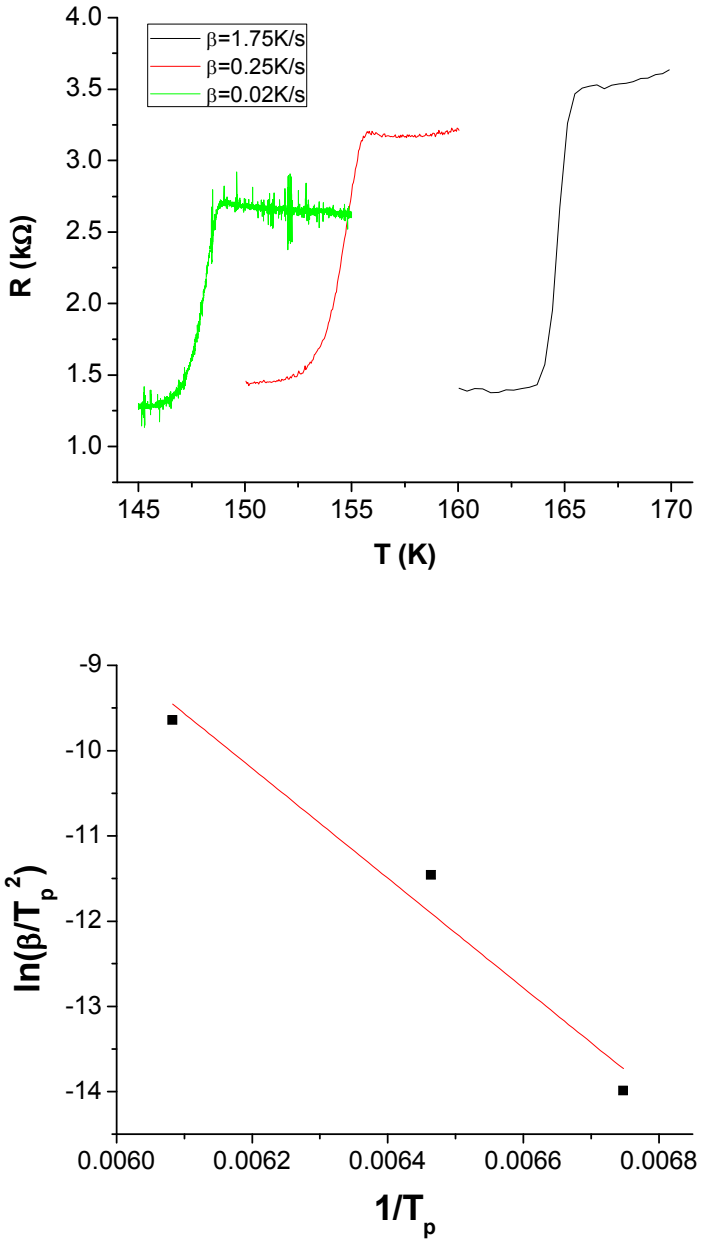

Figure 6.3 Temperature programmed desorption of K/ice from graphene. (top) Resistance vs. temperature for three different heating rates β as given in the legend, used to determine the desorption peak temperature T_p. (bottom) Plot of $\ln(\beta/T_p^2)$ vs $1/T_p$. The slope gives the activation energy $E_a = 0.55$ eV.

The potassium desorption data proves that ice plays an important role in desorption of coadsorbed ice and potassium.

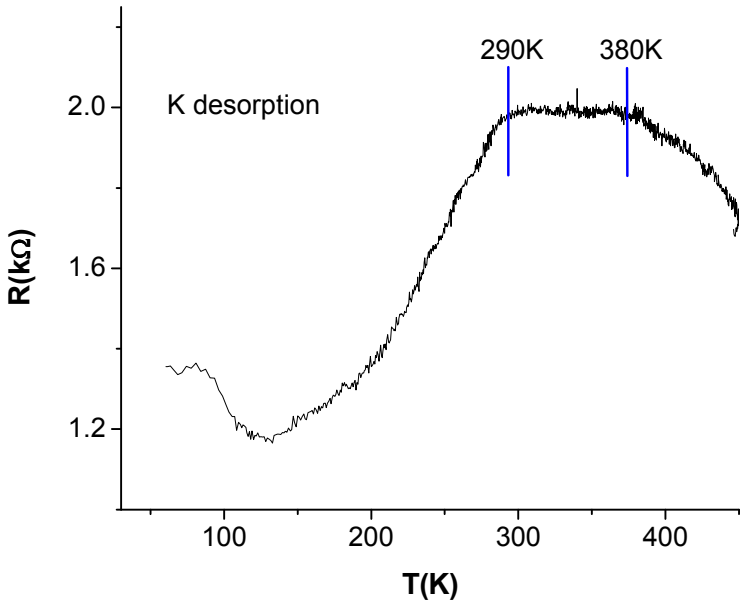

Figure 6.4 Desorption of dilute potassium. Doping changes in a slow manner and at higher temperature than in the case of coadsorption of ice and dilute potassium.

6.2 Desorption of ice

In the coadsorption experiments above, I observed that graphene devices have very low mobility after ice desorption. (In Figure 6.1, at 148K the mobility is ~ 4600 $cm^2v^{-1}s^{-1}$, which is much lower than the mobility of the device at pristine state $\mu \sim 19{,}000$ $cm^2v^{-1}s^{-1}$.) Given the low doping, it is difficult to explain the low mobility as due to scattering by charged impurities. Other surface processes may be responsible for it, e.g., the dissociation of ice molecules at desorption, which may create covalent bonding on structural defect sites on the graphene.

For comparison, I studied the behavior of graphene devices that are only covered with ice overlayers and no potassium. Figure 6.5 shows the temperature programmed desorption of ice with different initial coverages deposited at 40 K. Sharp changes in the resistivity vs. temperature are seen similar to the features observed in the coadsorption

experiments. The data with 1ML of ice shows that there is a rise in resistance at around 120K, where the temperature is too low for ice to desorb. In the 8 ML data the same feature appears shifted to 145 K, and similar to the feature observed at the same temperature in the K/ice coadsorption experiments (Figure 6.2). If the feature represents a similar physical change in ice overlayers, it would indicate a phase transition rather than desorption. For 8 ML of ice the amorphous to crystalline phase transition is expected at similar temperature; and for 1 ML of ice, another phase transition, amorphous to wetting 2-layer (observed in Ref. [72] at 120K) transition occurs at a temperature similar to the observed resistance increase. The 3 ML data set appears to be a crossover between these two types of transitions (perhaps exhibiting both transitions in different spatially separated regions).

Figure 6.6 shows the TPD of 8 ML of ice measured in the same way as in the K/ice coadsorption experiments (see Figure 6.3). An activation energy E_a is fit using X and Y data in Table 6.2. $E_a = 0.50$eV is very close to the result in coadsorption systems.

Peak Temperature (K)	Heating Rate (K/s)	$Y = ln(\beta/T_p^2)$	$X = 1/T_p$
145.8	0.02056	0.00686	-13.8489
153	0.1022	0.00654	-12.3417
159.1	0.72153	0.00629	-10.4655

Table 6.2 Fitting variables X and Y for ice desorption experiments.

Before each ice adsorption experiment, graphene devices are prepared in the pristine state with very low doping. Surprisingly, I found that the introduction of ice through the leak valve and adsorption of ice on graphene was accompanied by *p*-type doping, which keeps shifting the minimum conductivity to the positive direction in gate voltage at low temperatures (see Figure 6.5 bottom panel).

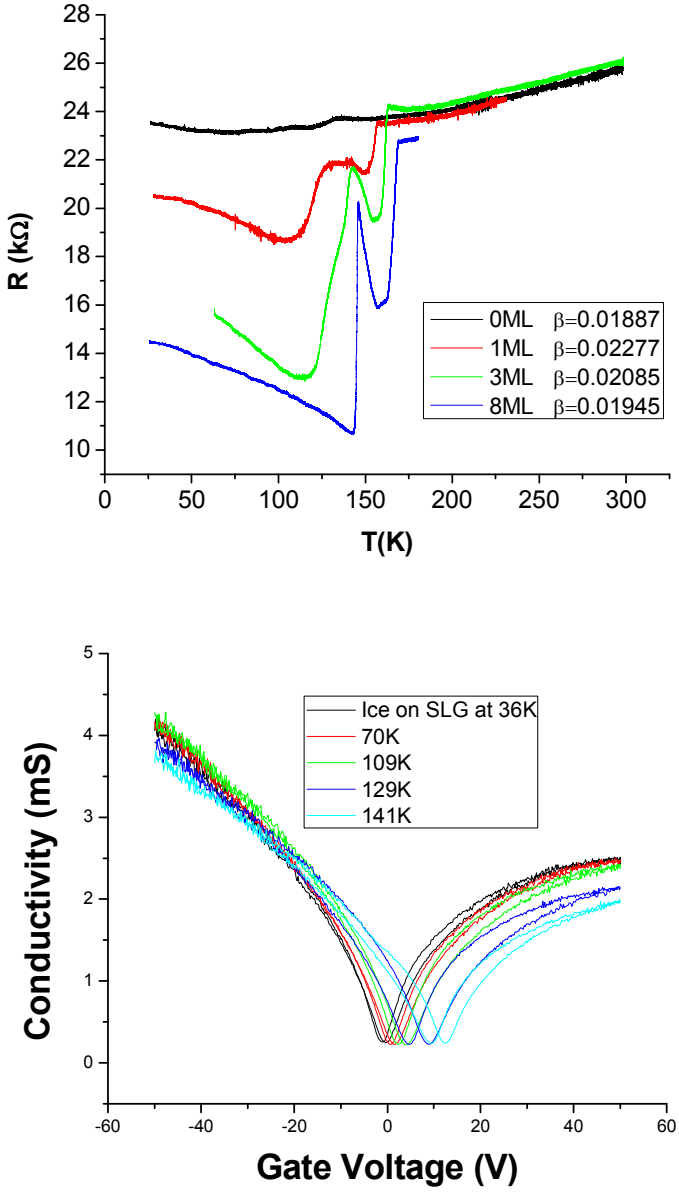

Figure 6.5 Desorption of ice (top). Resistance vs. temperature is shown for graphene with ice deposited at 40 K at different coverages indicated in legend. Temperature is ramped at the rate β given in the legend. Doping effects (bottom). After deposition of ice at 36 K on SLG, a strong doping effect is observed during warmup. Different colors represent different temperatures as indicated in legend. The shift of minimum conductivity explains the initial decrease in resistance in the top panel.

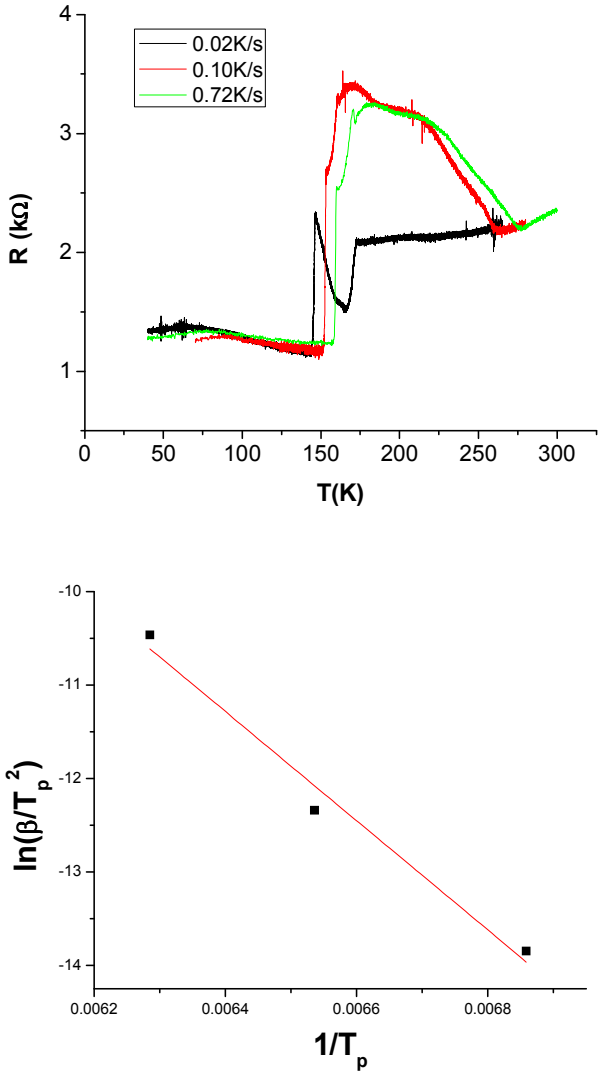

Figure 6.6 Temperature programmed desorption of ice from graphene. (top) Resistance vs. temperature for three different heating rates β as given in the legend, used to determine the desorption peak temperature T_p. (bottom) Plot of $\ln(\beta/T_p^2)$ vs $1/T_p$. The slope gives the activation energy $E_a = 0.50$ eV.

The water introduced into the UHV chamber has undergone several freeze-pump-thaw cycles to purify it and remove dissolved gases. However it is not entirely pure. I observe a partial pressure of 1×10^{-10} *Torr* of oxygen when the water partial pressure reaches 1×10^{-8} *Torr* . Such a small amount of oxygen impurity cannot be removed from

the water, but was not expected to dope the graphene[39, 73-76]. However, the observation of doping during water adsorption indicates that oxygen impurities coadsorbed with ice may dope graphene. This is explored further below.

6.3 Adsorption and desorption of molecular oxygen

There have been several experiments demonstrating the doping effect of molecular oxygen adsorbed on graphene and carbon nanotubes at atmospheric pressure[39, 73-76]. In this section, oxygen adsorption on clean graphene is studied under a well-controlled environment. Surprisingly, the electronic properties of graphene are extremely sensitive to oxygen at low temperature.

Adsorption of oxygen molecules on graphene has been widely studied on graphite and carbon nanotubes[71]. In our experiments, pure oxygen is introduced into the UHV chamber through a leak valve and some oxygen molecules (sticking coefficient < 1) are frozen on clean graphene surface at low temperature (lower than the oxygen desorption temperature of 40 K[71]).

Figure 6.7 (top) shows an oxygen doping experiment at 45K. For oxygen partial pressures up to $1\times10^{-8}\,Torr$, there is no doping effect (no shift in $V_{g,min}$). For oxygen pressure of $2.5\times10^{-8}\,Torr$, clear doping effects (shift in $V_{g,min}$) start to appear. Interestingly, the doping appears to be activated by sweeping the gate voltage. A shift in $V_{g,min}$ is evident in the second gate sweeping. In the last doping at $7.6\times10^{-8}\,Torr$, there are strong doping effects in the first gate sweeping and second sweeping incurs more doping. And the doping saturates in the third gate sweeping. The saturated shift in $V_{g,min}$ of ~15 V corresponds to a carrier concentration of $\sim10^{12}$ cm^{-2}, or one dopant per 5000

carbon atoms. This doping level is orders of magnitude smaller than the oxygen molecule exposure of the surface.

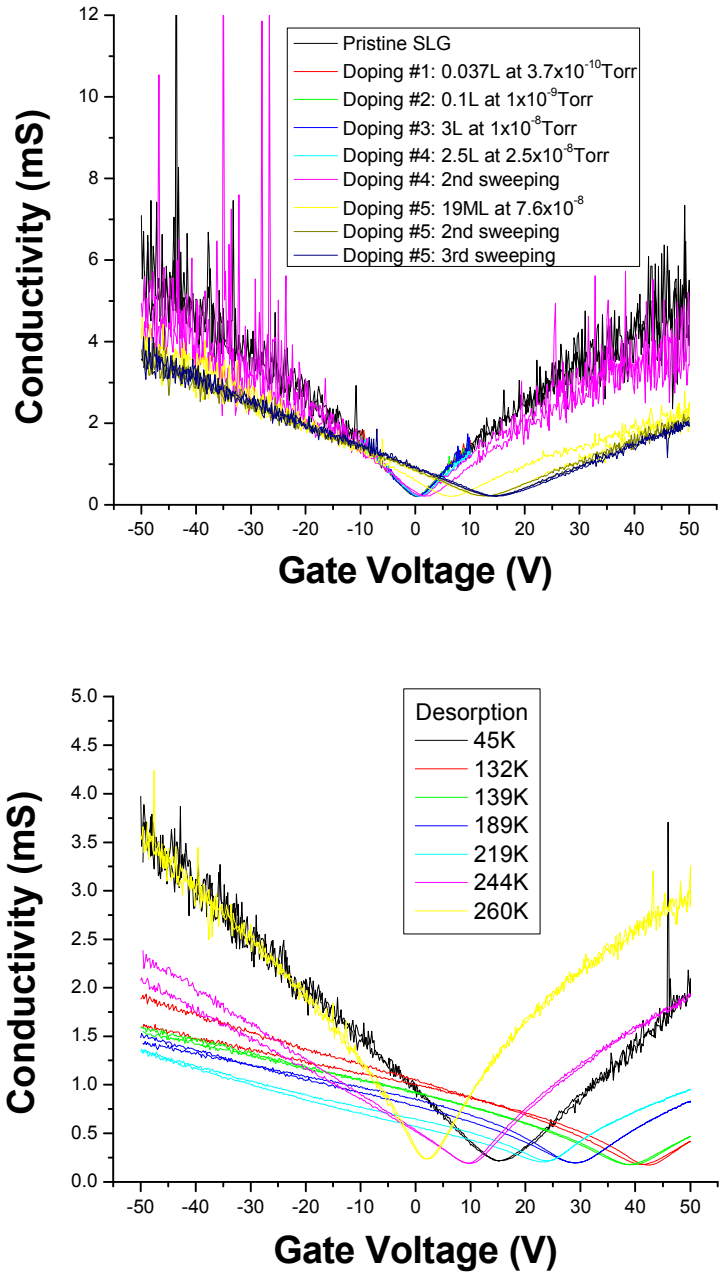

Figure 6.7 Adsorption of oxygen at 30K (top). The amount of oxygen introduced into the UHV chamber is given in the legend. Desorption of oxygen (bottom) at warmup. Different colors represent different temperatures as indicated in the legend. At temperatures below 130 K, doping keeps increasing. Above 130 K, doping gradually decreases.

Upon warmup, the doping increases with temperature much more until ~130K. This is quite surprising, since oxygen molecules desorb at ~40 K. I theorize that the doping behavior comes from residual oxygen which remains after desorption, which must be chemisorbed to the graphene, possibly to defect sites. Doping decreases at higher temperatures, and at 260 K the graphene device is restored to its original low doping state. The oxygen desorption experiments bear certain similarities with the ice desorption experiments: the increasing doping during warmup, low mobility of graphene devices and decreasing doping after certain temperatures. The gate sweeping activated doping and the residue oxygen doping effect may be related to the second resistance increase in ice desorption experiments.

Oxygen partial pressure (Torr)	Oxygen coverage (L)	Water partial pressure (Torr)	Ice coverage (L)	Adsorption temperature (K)	ΔV_d at adsorption temperature (V)	Maximum ΔV_d during warmup
$1x10^{-10}$	0	$2.5x10^{-08}$	9	49	2	6.5
$1x10^{-08}$	3.5	$1.5x10^{-08}$	3	47	2.5	8
$6x10^{-08}$	12	$5x10^{-08}$	10	48	5.5	14
$6x10^{-08}$	12	$4x10^{-10}$	0	46	1.5	8

Table 6.3 Interaction of ice and oxygen on graphene.

To understand the interaction of ice and oxygen adsorbates on graphene, I studied the doping effect with different ice and oxygen coverages, which are introduced into the UHV chamber simultaneously through two different leak valves. Without ice, 3 Langmuir (L; 1 L corresponds to 10^{-6} *Torr* exposure during 1 second.) of oxygen at 1×10^{-8} *Torr* do not dope graphene (see Figure 6.7). When similar dose of oxygen coadsorbs with 3 L of ice, a strong doping effect is observed (see Table 6.3). This process may involve ice and oxygen reaction that induces chemical adsorption of oxygen, which

can explain the doping of ice with oxygen impurities. However, the observation of doping with dry oxygen indicates that there is also a defect-induced chemisorption process.

6.4. Summary

In this chapter, I summarize the experimental results related to the temperature-dependent phenomena of coadsorbed potassium and ice. For graphene devices with coadsorbed potassium and ice at low temperatures, an increase of the mobility is seen upon warming, which is qualitatively explain by solvation of the potassium ions by ice. Upon further warming of graphene with ice, or coadsorbed ice and potassium, sudden shifts in the conductivity, reflecting sudden changes in doping, are observed. A shift in doping at 140 K is observed for graphene with ice adsorbed ice and coadsorbed ice/potassium, and may mark a structural phase transition in the ice from disordered 2D film to crystalline 3D ice which dewets the surface. The transition may be accompanied by desorption of potassium, or in the case of ice adsorption only, desorption of molecular oxygen which is present as an impurity in the water introduced to the chamber. Intentional adsorption of molecular oxygen or coadsorption of oxygen and ice is found to enhance the *p*-type doping and confirms that molecular oxygen is a dopant on graphene. Surprisingly, oxygen doping persists on graphene to high temperatures (~260 K), much higher than necessary to remove physisorbed oxygen on graphite, suggesting that the chemisorption of oxygen associated with doping of the graphene may be mediated by defects in the graphene itself.

Chapter 7 Summary

In this thesis, two main subjects are discussed: the scattering mechanism in bilayer graphene, and detection of physical and chemical processes on the graphene surface with electronic signals.

I have examined the impact of charged impurity scattering on charge carrier transport in bilayer graphene by deposition of potassium in UHV at low temperature. Charged impurity scattering gives a conductivity which is supra-linear in carrier density, with a magnitude similar to single-layer graphene for the measured range of carrier densities of 2-4 x 10^{12} cm^{-2}. Upon addition of charged impurities of concentration n_{imp}, the minimum conductivity σ_{min} decreases proportional to $n_{imp}^{-1/2}$, while the electron and hole puddle carrier density increases proportional to $n_{imp}^{1/2}$. These results for the intentional deposition of potassium on bilayer graphene are consistent with theoretical predictions for charged impurity scattering assuming a gapless hyperbolic dispersion relation. I discovered that the scattering cross section of charged impurity is similar in bilayer and single layer graphene. However, my results also indicate that charged impurity scattering alone cannot explain the observed transport properties of pristine bilayer on SiO_2 (i.e. without potassium doping), which is supported by further experiments on dielectric screening of pristine bilayer graphene and K-doped bilayer graphene. The carrier scattering mechanism in pristine bilayer graphene remains unknown.

Various physical and chemical surface phenomena have been studied on the surface of graphene. Coadsorption of ice and dilute potassium demonstrates that microscopic process, such as solvation, can be detected by an electronic signal from

graphene devices. Desorption of coadsorbed ice and dilute potassium shows similar features as desorption of ice, and reflects phase transitions in the ice overlayers. Adsorption and desorption of oxygen provide rich information that is related to the observed doping shifts in desorption experiments.

Electronic signals from graphene can be used to study various surface science phenomena. Comparing to conventional surface science techniques (for example, low energy electron diffraction), it has several advantages. First, it generates a fast response. It can provide real-time information about the graphene-adsorbate interface. Second, it has a fine spatial resolution since electrical readout of graphene devices is possible in the deep sub-micron regime. Thus, graphene devices could be used to study size-dependent phenomena. Third, it is very sensitive to the graphene-adsorbate interface even when the interface is buried under thick adsorbates. As demonstrated in the experiments of coadsorbed potassium and ice, electronic signals have been used to estimate the size of the hydration shells under 10ML of ice.

In the future, I expect that other experiments can help to unravel the complex processes in desorption. In our experimental setup, the RGA can only measure the gas desorption from the whole cold finger and during desorption the vacuum chamber can not be kept at UHV. A pinhole doser, combined with the use of larger-area graphene devices (such as graphene prepared by chemical vapor deposition which may be cm-sized) can constrain the adsorbates to the graphene surface and keep the chamber in UHV through adsorption and desorption cycles. Using the shift of $V_{g,min}$ to calculate the carrier density is not always reliable and requires gate sweeping which is time consuming. Simultaneous measurement of longitudinal and Hall conductivities would measure both the mobility

and the carrier concentration (doping) and could be performed rapidly without gate sweeping, therefore providing a real time sampling of carrier density, which would be much better than the resistance sampling alone. Such measurements could be carried out during temperature-programmed desorption, for example, to study independently the changes in doping and mobility.

Finally, the transport measurements presented here can only provide indirect information of the state of graphene's surface. Other direct techniques such as low-energy electron diffraction (LEED) or low temperature AFM can monitor the actual adsorption and desorption process and provide an independent measurement to compare with the information gained from transport studies.

Bibliography

1. Wallace, P.R., *The Band Theory of Graphite.* Physical Review, 1947. **71**(9): p. 622-634.
2. DiVincenzo, D.P. and E.J. Mele, *Self-consistent effective-mass theory for intralayer screening in graphite intercalation compounds.* Physical Review B, 1984. **29**(4): p. 1685-1694.
3. Semenoff, G.W., *Condensed-Matter Simulation of a Three-Dimensional Anomaly.* Physical Review Letters, 1984. **53**(26): p. 2449-2452.
4. Novoselov, K.S., et al., *Electric Field Effect in Atomically Thin Carbon Films.* Science, 2004. **306**(5696): p. 666-669.
5. Ebbesen, T.W. and H. Hiura, *Graphene in 3-dimensions: Towards graphite origami.* Advanced Materials, 1995. **7**(6): p. 582-586.
6. Zhang, Y.B., et al., *Electric field modulation of galvanomagnetic properties of mesoscopic graphite.* Physical Review Letters, 2005. **94**(17).
7. Bunch, J.S., et al., *Coulomb Oscillations and Hall Effect in Quasi-2D Graphite Quantum Dots.* Nano Letters, 2005. **5**(2): p. 287-290.
8. Xuekun Lu, M.Y., Hui Huang and Rodney. S. Ruoff, *Tailoring graphite with the goal of achieving single sheets.* Nanotechnology, 1999. **10**(3): p. 269.
9. Novoselov, K.S., et al., *Two-dimensional gas of massless Dirac fermions in graphene.* Nature, 2005. **438**(7065): p. 197-200.
10. Zhang, Y., et al., *Experimental observation of the quantum Hall effect and Berry's phase in graphene.* Nature, 2005. **438**(7065): p. 201-204.
11. Andrei, E.Y., G.H. Li, and X. Du, *Electronic properties of graphene: a perspective from scanning tunneling microscopy and magnetotransport.* Reports on Progress in Physics, 2012. **75**(5).
12. Bolotin, K.I., et al., *Ultrahigh electron mobility in suspended graphene.* Solid State Communications, 2008. **146**(9-10): p. 351-355.
13. Nair, R.R., et al., *Fine structure constant defines visual transparency of graphene.* Science, 2008. **320**(5881): p. 1308-1308.
14. Stander, N., B. Huard, and D. Goldhaber-Gordon, *Evidence for Klein Tunneling in Graphene p-n Junctions.* Physical Review Letters, 2009. **102**(2): p. 026807.
15. Balandin, A.A., et al., *Superior thermal conductivity of single-layer graphene.* Nano Letters, 2008. **8**(3): p. 902-907.
16. Garaj, S., et al., *Graphene as a subnanometre trans-electrode membrane.* Nature, 2010. **467**(7312): p. 190-U73.
17. Miller, J.R., R.A. Outlaw, and B.C. Holloway, *Graphene electric double layer capacitor with ultra-high-power performance.* Electrochimica Acta, 2011. **56**(28): p. 10443-10449.
18. Xia, F.N., et al., *Photocurrent Imaging and Efficient Photon Detection in a Graphene Transistor.* Nano Letters, 2009. **9**(3): p. 1039-1044.
19. Ju, L., et al., *Graphene plasmonics for tunable terahertz metamaterials.* Nature Nanotechnology, 2011. **6**(10): p. 630-634.
20. *Nanotechnology: Graphene touch.* Nature, 2010. **465**(7301): p. 988-988.

21. Geim, A.K., *Graphene: Status and Prospects.* Science, 2009. **324**(5934): p. 1530-1534.
22. Michael S. Fuhrer, C.N.L., and Allan H. MacDonald *Graphene: Materially Better Carbon* MRS Bulletin, 2010. **35**: p. 289-295.
23. Das Sarma, S. and E.H. Hwang, *Charged Impurity-Scattering-Limited Low-Temperature Resistivity of Low-Density Silicon Inversion Layers.* Physical Review Letters, 1999. **83**(1): p. 164-167.
24. Das Sarma, S. and E.H. Hwang, *Metallicity and its low-temperature behavior in dilute two-dimensional carrier systems.* Physical Review B, 2004. **69**(19): p. 195305.
25. Ando, T., A.B. Fowler, and F. Stern, *Electronic properties of two-dimensional systems.* Reviews of Modern Physics, 1982. **54**(2): p. 437-672.
26. Adam, S., et al., *A self-consistent theory for graphene transport.* Proceedings of the National Academy of Sciences, 2007. **104**(47): p. 18392-18397.
27. Hwang, E.H. and S. Das Sarma, *Dielectric function, screening, and plasmons in two-dimensional graphene.* Physical Review B, 2007. **75**(20): p. 205418.
28. Adam, S., E.H. Hwang, and S. Das Sarma, *Scattering mechanisms and Boltzmann transport in graphene.* Physica E: Low-dimensional Systems and Nanostructures, 2008. **40**(5): p. 1022-1025.
29. Yan, J. and M.S. Fuhrer, *Correlated Charged Impurity Scattering in Graphene.* Physical Review Letters, 2011. **107**(20).
30. McCann, E. and V.I. Fal'ko, *Landau-level degeneracy and quantum hall effect in a graphite bilayer.* Physical Review Letters, 2006. **96**(8).
31. Adam, S. and S. Das Sarma, *Boltzmann transport and residual conductivity in bilayer graphene.* Physical Review B, 2008. **77**(11).
32. Novoselov, K.S., et al., *Two-dimensional atomic crystals.* Proceedings of the National Academy of Sciences of the United States of America, 2005. **102**(30): p. 10451-10453.
33. Ferrari, A.C., *Raman spectroscopy of graphene and graphite: Disorder, electron-phonon coupling, doping and nonadiabatic effects.* Solid State Communications, 2007. **143**(1-2): p. 47-57.
34. Malard, L.M., et al., *Raman spectroscopy in graphene.* Physics Reports, 2009. **473**(5-6): p. 51-87.
35. Ferrari, A.C., et al., *Raman spectrum of graphene and graphene layers.* Physical Review Letters, 2006. **97**(18).
36. Lenski, D.R. and Fuhrer, M.S., *Raman and optical characterization of multilayer turbostratic graphene grown via chemical vapor deposition.* Journal of Applied Physics, 2011. **110**(1): p. 013720.
37. Ishigami, M., et al., *Atomic structure of graphene on SiO2.* Nano Letters, 2007. **7**(6): p. 1643-1648.
38. Collins, P.G., et al., *Extreme oxygen sensitivity of electronic properties of carbon nanotubes.* Science, 2000. **287**(5459): p. 1801-1804.
39. Levesque, P.L., et al., *Probing Charge Transfer at Surfaces Using Graphene Transistors.* Nano Letters, 2011. **11**(1): p. 132-137.
40. Cui, X.D., et al., *Controlling energy-level alignments at carbon nanotube/Au contacts.* Nano Letters, 2003. **3**(6): p. 783-787.

41. Redhead, P.A., *Thermal desorption of gases.* Vacuum, 1962. **12**(4): p. 203-211.
42. Novoselov, K.S., et al., *Unconventional quantum Hall effect and Berry's phase of 2 pi in bilayer graphene.* Nature Physics, 2006. **2**(3): p. 177-180.
43. Nilsson, J., et al., *Electronic properties of bilayer and multilayer graphene.* Physical Review B, 2008. **78**(4).
44. Mak, K.F., et al., *Observation of an Electric-Field-Induced Band Gap in Bilayer Graphene by Infrared Spectroscopy.* Physical Review Letters, 2009. **102**(25).
45. McCann, E., *Asymmetry gap in the electronic band structure of bilayer graphene.* Physical Review B, 2006. **74**(16).
46. Oostinga, J.B., et al., *Gate-induced insulating state in bilayer graphene devices.* Nature Materials, 2008. **7**(2): p. 151-157.
47. Zhang, Y.B., et al., *Direct observation of a widely tunable bandgap in bilayer graphene.* Nature, 2009. **459**(7248): p. 820-823.
48. Zhao, Y., et al., *Symmetry Breaking in the Zero-Energy Landau Level in Bilayer Graphene.* Physical Review Letters, 2010. **104**(6): p. 066801.
49. McCann, E. and M. Koshino, *The electronic properties of bilayer graphene.* 2012, arXiv:1205.6953v1.
50. Morozov, S.V., et al., *Giant intrinsic carrier mobilities in graphene and its bilayer.* Physical Review Letters, 2008. **100**(1).
51. Katsnelson, M.I., *Scattering of charge carriers by point defects in bilayer graphene.* Physical Review B, 2007. **76**(7): p. 073411.
52. Koshino, M. and T. Ando, *Transport in bilayer graphene: Calculations within a self-consistent Born approximation.* Physical Review B, 2006. **73**(24): p. 245403.
53. Chen, J.H., et al., *Diffusive charge transport in graphene on SiO(2).* Solid State Communications, 2009. **149**(27-28): p. 1080-1086.
54. Chen, J.H., et al., *Charged-impurity scattering in graphene.* Nature Physics, 2008. **4**(5): p. 377-381.
55. Hwang, E.H., S. Adam, and S. Das Sarma, *Carrier transport in two-dimensional graphene layers.* Physical Review Letters, 2007. **98**(18).
56. Jang, C., et al., *Tuning the effective fine structure constant in graphene: Opposing effects of dielectric screening on short- and long-range potential scattering.* Physical Review Letters, 2008. **101**(14).
57. Caragiu, M. and S. Finberg, *Alkali metal adsorption on graphite: a review.* Journal of Physics-Condensed Matter, 2005. **17**(35): p. R995-R1024.
58. Hwang, E.H. and S. Das Sarma, *Screening, Kohn Anomaly, Friedel Oscillation, and RKKY Interaction in Bilayer Graphene.* Physical Review Letters, 2008. **101**(15).
59. Ando, T., *Screening effect and impurity scattering in monolayer graphene.* Journal of the Physical Society of Japan, 2006. **75**(7).
60. Pal, A.N. and A. Ghosh, *Resistance Noise in Electrically Biased Bilayer Graphene.* Physical Review Letters, 2009. **102**(12).
61. Lin, Y.M. and P. Avouris, *Strong suppression of electrical noise in bilayer graphene nanodevices.* Nano Letters, 2008. **8**(8): p. 2119-2125.
62. S. Das Sarma, E.H. Hwang, and E. Rossi, *Theory of carrier transport in bilayer graphene.* Physical Review B, 2010. **81**(16): p. 161407.

63. Xiao, S.D., et al., *Charged impurity scattering in bilayer graphene.* Physical Review B, 2010. **82**(4).
64. Henderson, M.A., *The interaction of water with solid surfaces: fundamental aspects revisited.* Surface Science Reports, 2002. **46**(1-8): p. 1-308.
65. Chakarov, D.V., L. Osterlund, and B. Kasemo, *Water-Adsorption and Coadsorption with Potassium on Graphite(0001).* Langmuir, 1995. **11**(4): p. 1201-1214.
66. Sheng, M., et al., *Two-dimensional hydration shells of alkali metal ions at a hydrophobic surface.* The Journal of Chemical Physics, 2004. **121**(24): p. 12572-12576.
67. Bornemann, T., et al., *The Adsorption of H2o on K Precovered Ni(111) Studied by Arups and Tpd.* Surface Science, 1991. **254**(1-3): p. 105-118.
68. Dean, C.R., et al., *Boron nitride substrates for high-quality graphene electronics.* Nature Nanotechnology, 2010. **5**(10): p. 722-726.
69. Chakarov, D.V., L. Österlund, and B. Kasemo, *Water adsorption on graphite (0001).* Vacuum, 1995. **46**(8-10): p. 1109-1112.
70. Bolina, A.S., A.J. Wolff, and W.A. Brown, *Reflection Absorption Infrared Spectroscopy and Temperature-Programmed Desorption Studies of the Adsorption and Desorption of Amorphous and Crystalline Water on a Graphite Surface.* The Journal of Physical Chemistry B, 2005. **109**(35): p. 16836-16845.
71. Ulbricht, H., et al., *Thermal desorption of gases and solvents from graphite and carbon nanotube surfaces.* Carbon, 2006. **44**(14): p. 2931-2942.
72. Kimmel, G.A., et al., *No Confinement Needed: Observation of a Metastable Hydrophobic Wetting Two-Layer Ice on Graphene.* Journal of the American Chemical Society, 2009. **131**(35): p. 12838-12844.
73. Sato, Y., K. Takai, and T. Enoki, *Electrically Controlled Adsorption of Oxygen in Bilayer Graphene Devices.* Nano Letters, 2011. **11**(8): p. 3468-3475.
74. Yang, Y.X., K. Brenner, and R. Murali, *The influence of atmosphere on electrical transport in graphene.* Carbon, 2012. **50**(5): p. 1727-1733.
75. Yang, Y.X. and R. Murali, *Binding mechanisms of molecular oxygen and moisture to graphene.* Applied Physics Letters, 2011. **98**(9).
76. Zhou, H.Q., et al., *Raman scattering of monolayer graphene: the temperature and oxygen doping effects.* Journal of Physics D-Applied Physics, 2011. **44**(18).